

Bottom-up inputs are required for establishment of top-down connectivity onto cortical layer 1 neurogliaform cells

Highlights

- During development, L1 NGF cells receive strong dLGN inputs but weak ACC connectivity
- ACC inputs onto L1 NGF cells, but not onto “canopy” cells, strengthen in the adult
- Sensory deprivation blocked the strengthening of ACC afferents onto L1 NGF cells
- Early ACC is strengthened precociously by stimulation in a thalamus-dependent manner

Authors

Leena Ali Ibrahim, Shuhan Huang, Marian Fernandez-Otero, ..., Gabrielle Pouchelon, Bernardo Rudy, Gord Fishell

Correspondence

gordon_fishell@hms.harvard.edu (G.F.),
leena.ibrahim@kaust.edu.sa (L.A.I.)

In brief

During development in the visual cortex, there is a shift in the flow of information processing from predominately bottom-up to top-down. Ibrahim et al. show that the strength of thalamic inputs onto layer 1 interneurons directly affects development of connectivity of these cells from the anterior cingulate cortex.



Article

Bottom-up inputs are required for establishment of top-down connectivity onto cortical layer 1 neurogliaform cells

Leena Ali Ibrahim,^{1,2,7,*} Shuhan Huang,^{1,2,3} Marian Fernandez-Otero,^{1,2} Mia Sherer,^{1,6} Yanjie Qiu,^{1,2} Spurti Vemuri,⁶ Qing Xu,⁵ Robert Machold,⁴ Gabrielle Pouchelon,¹ Bernardo Rudy,⁴ and Gord Fishell^{1,2,8,*}

¹Harvard Medical School, Blavatnik Institute, Department of Neurobiology, Boston, MA, USA

²Broad Institute, Stanley Center for Psychiatric Research, Cambridge, MA, USA

³Program in Neuroscience, Harvard Medical School, Boston, MA, USA

⁴Neuroscience Institute, New York University School of Medicine, New York, NY, USA

⁵Center for Genomics & Systems Biology, New York University, Abu Dhabi, UAE

⁶Northeastern University, Boston, MA, USA

⁷King Abdullah University of Science and Technology (KAUST), Thuwal, Saudi Arabia

⁸Lead contact

*Correspondence: gordon_fishell@hms.harvard.edu (G.F.), leena.ibrahim@kaust.edu.sa (L.A.I.)

<https://doi.org/10.1016/j.neuron.2021.08.004>

SUMMARY

Higher-order projections to sensory cortical areas converge on layer 1 (L1), the primary site for integration of top-down information via the apical dendrites of pyramidal neurons and L1 GABAergic interneurons. Here we investigated the contribution of early thalamic inputs onto L1 interneurons for establishment of top-down connectivity in the primary visual cortex. We find that bottom-up thalamic inputs predominate during L1 development and preferentially target neurogliaform cells. We show that these projections are critical for the subsequent strengthening of top-down inputs from the anterior cingulate cortex onto L1 neurogliaform cells. Sensory deprivation or selective removal of thalamic afferents blocked this phenomenon. Although early activation of the anterior cingulate cortex resulted in premature strengthening of these top-down afferents, this was dependent on thalamic inputs. Our results demonstrate that proper establishment of top-down connectivity in the visual cortex depends critically on bottom-up inputs from the thalamus during postnatal development.

INTRODUCTION

Our capacity to perceive and react to a rapidly changing world relies on the ability of the neocortex to respond accurately and precisely to sensory stimuli in a dynamic environment. Processing sensory information, such as vision, depends critically on our ability to attend to stimuli, filter distractors, and accurately make predictions about our surroundings (Desimone and Duncan, 1995; Rao and Ballard, 1999; Kastner and Ungerleider, 2000; Ardid et al., 2007; Squire et al., 2013; Zhang et al., 2014; Huda et al., 2020). Integration of top-down feedback from higher-order brain areas and incoming sensory signals allows for such functions. Cortical inhibitory interneurons (INs) have been increasingly implicated in this process. Although parvalbumin (PV), somatostatin (SST), and vasoactive intestinal peptide (VIP) INs have been posited to contribute to such computations (Lee et al., 2013; Fu et al., 2014; Zhang et al., 2014; Leinweber et al., 2017; Schneider et al., 2018), the involvement of L1 INs has been less explored. L1 contains dense axonal projections from various brain regions and is, in fact, the main target of corticocortical projections from diverse cortical areas as well

as thalamocortical projections (Oh et al., 2014; Zingg et al., 2014; Schuman et al., 2021). These projections not only target the distal apical dendrites of pyramidal neurons but also the INs located within layer 1 (L1) (Ibrahim et al., 2020). Importantly, L1 INs have been shown to receive thalamic (Ji et al., 2016) and intercortical connections (Leinweber et al., 2017; Cohen-Kashi Malina et al., 2021; Naskar et al., 2021). This ideally positions them to modulate incoming sensory inputs and regulate excitatory responses (Zhu and Zhu, 2004; Jiang et al., 2013; Lee et al., 2015; Anastasiades et al., 2020; Cohen-Kashi Malina et al., 2021). L1 INs have also been shown to play a role in cross-modal integration (Ibrahim et al., 2016), interhemispheric inhibition (Palmer et al., 2012), associative fear learning and plasticity (Abs et al., 2018; Pardi et al., 2020), as well as sensory motor integration (Mesik et al., 2019). These findings implicate L1 INs as a critical nexus for integration of bottom-up and top-down signaling.

A considerable breadth of evidence supports the idea that activity in the early postnatal cortex is initially dominated by bottom-up signals. The cortex develops recurrent activity only later, following establishment of functional connectivity between



primary and associative cortical areas (Colonnese et al., 2010; Luhmann and Khazipov, 2018; Dominguez et al., 2021). These findings suggest that emergence of cortical function is a sequential process that relies on distinct epochs of activity. Although it is well established that sensory experience plays a crucial role in excitatory and inhibitory neuron development (Chou et al., 2013; Pouchelon et al., 2014; De Marco Garcia et al., 2015), whether it is required for establishment of top-down circuits is not known.

The two largest populations of L1 INs are neurogliaform (NGF) and “canopy” cells, both of which express neuron-derived neurotrophic factor (NDNF Schuman et al., 2019). Here we explore development of the afferent connectivity to these cell types in the primary visual cortex (V1) and reveal that they exhibit significant differences in when they receive afferent inputs. Using monosynaptic rabies tracing, we find that bottom-up thalamic inputs dominate during development, whereas top-down inputs are strengthened progressively later in development. Our results show that, early in development, L1 NGF cells are the main recipients of thalamic inputs. In contrast, canopy cells in L1 only receive thalamic afferents at later ages. Moreover, we find that bottom-up inputs from the dorsal lateral geniculate nucleus (dLGN) onto L1 NGF cells are required for later establishment of corticocortical top-down afferents from the anterior cingulate cortex (ACC). This region that has been implicated in visual discrimination (Zhang et al., 2014; Huda et al., 2020) and visuo-motor mismatch responses (Attinger et al., 2017; Leinweber et al., 2017) through their projections to V1. Specifically, we observe that enucleation or ablation of thalamic inputs to L1 INs prevents strengthening of ACC afferents onto them. Conversely, premature activation of the ACC inputs results in precocious development of ACC input strength onto NGF cells, a phenomenon that is critically dependent on the thalamus. These findings demonstrate the importance of bottom-up thalamic inputs on development of top-down connectivity from the ACC onto L1 NGF INs in V1.

RESULTS

Developing L1 INs switch from receiving predominantly bottom-up thalamic to receiving top-down corticocortical afferents

To map L1 INs' monosynaptic afferent connectivity, we used the *NDNF-dgCre* driver mouse line (Tasic et al., 2016) to label canopy and L1 NGF cells, which together constitute ~70% of L1 INs (Tasic et al., 2018; Schuman et al., 2019; Ibrahim et al., 2020). In combination with a Cre-dependent AAV helper virus and a genetically modified CVS N2c strain of the G-deleted rabies (N2c-RV) (Figure 1A), we surveyed the monosynaptic input connectivity of these cells. This rabies strain has been found to be less toxic and more efficient in retrograde labeling of presynaptic cells than the originally used B19 version (Wickersham et al., 2007; Reardon et al., 2016). Cre-dependent expression of the AAV helper virus in NDNF cells provided the necessary components for infection of EnvA-pseudotyped rabies virus (TVA receptor) as well as for its replication and transport (G protein) (Figure 1A). All required helper components (i.e., N2c-G protein, TVA receptor, and EGFP reporter) were con-

tained within a single AAV virus (Pouchelon et al., 2020). AAV helper and N2c-RV-mCherry (RV) viruses were co-injected in V1. As expected, the starter cells (EGFP and mCherry co-expressing cells) were primarily localized within L1 (Figure 1B; Figure S1A). We used this approach at developmental and adult time points to compare the monosynaptic afferents onto L1 INs in V1.

To assess developmental connectivity, we injected the AAV helper and N2c-RV at post-natal day 1 (P1) and analyzed the retrogradely labeled cells at P15. For the adult connectivity, we injected mice at 4–5 weeks of age and analyzed the brains similarly 2 weeks later (Figure 1C). By quantifying the normalized number of retrogradely labeled neurons across regions (see STAR Methods for details), we found that, during development, the most numerous inputs L1 INs receive were from the sensory thalamus (i.e., the dLGN; Figures 1D and 1E; 0.471 ± 0.0217). In contrast, in adults, although L1 INs maintained thalamic inputs, they were collectively less numerous than the long-range corticocortical inputs from the ACC, premotor cortex (M2), and retrosplenial cortex (RSP) (Figure 1E, left panel; bottom-up proportion, 0.133 ± 0.016 ; top-down proportion, 0.478 ± 0.011). Interestingly, we found that ACC inputs increased more strongly from development to adulthood (~5-fold increase) compared with inputs from the RSP (~2-fold increase) (Figure 1E, right panel). We focused on these projections because they have been shown to have abundant axonal arbors in the superficial layers of V1. The increase in long-range corticocortical connectivity in the adult indicates that, as L1 INs mature, their afferents shift from being predominantly bottom up to top down. Additionally, L1 INs in V1 received local inputs, primarily from L5 and L6 (predominantly L6b) during development (Figure S1B, top; Meng et al., 2020) and from L5 (pyramidal neurons and presumably SST INs; Figure S1B, bottom; Abs et al., 2018) in the adult as well as long-range cortical inputs from higher visual areas (V2L/M), the auditory cortex (AUD), and the posterior parietal cortex (PTLp) (Figure 1F; Cohen-Kashi Malina et al., 2021). Interestingly, we observed a smaller but consistent projection to NDNF⁺ L1 INs from the contralateral ectorhinal cortex and ipsilateral *claustrum*. Furthermore, NDNF⁺ L1 INs received a small number of afferents from the basal forebrain and hypothalamic nuclei (Figure 1F).

NDNF⁺ L1 INs also received inputs from diverse thalamic nuclei (Figure 1F), such as the group of anterior thalamic nuclei (ATN) as well as the anterior pretectal nucleus (APN). Inputs from higher-order visual thalamic nuclei, such as the lateral-posterior nucleus (LP), and other visual thalamic nuclei, such as the lateral-dorsal nucleus (LD) (Nassi and Callaway, 2009; Saalman et al., 2012), were also very prominent. Interestingly, although the LP is thought to be the main source of thalamic inputs to L1 in V1 (Roth et al., 2016), based on our rabies tracing data, we found that dLGN inputs were more predominant onto NDNF⁺ cells during development and in the adult (Figure S1C, top and bottom).

L1 NGF cells and L4 excitatory cells receive dLGN inputs, some of which are shared

To label bottom-up thalamic afferents, we utilized the *Vipr2-Cre* driver line, which has been shown previously to be specifically expressed in the dLGN and not in the LP (Zhuang, 2019).

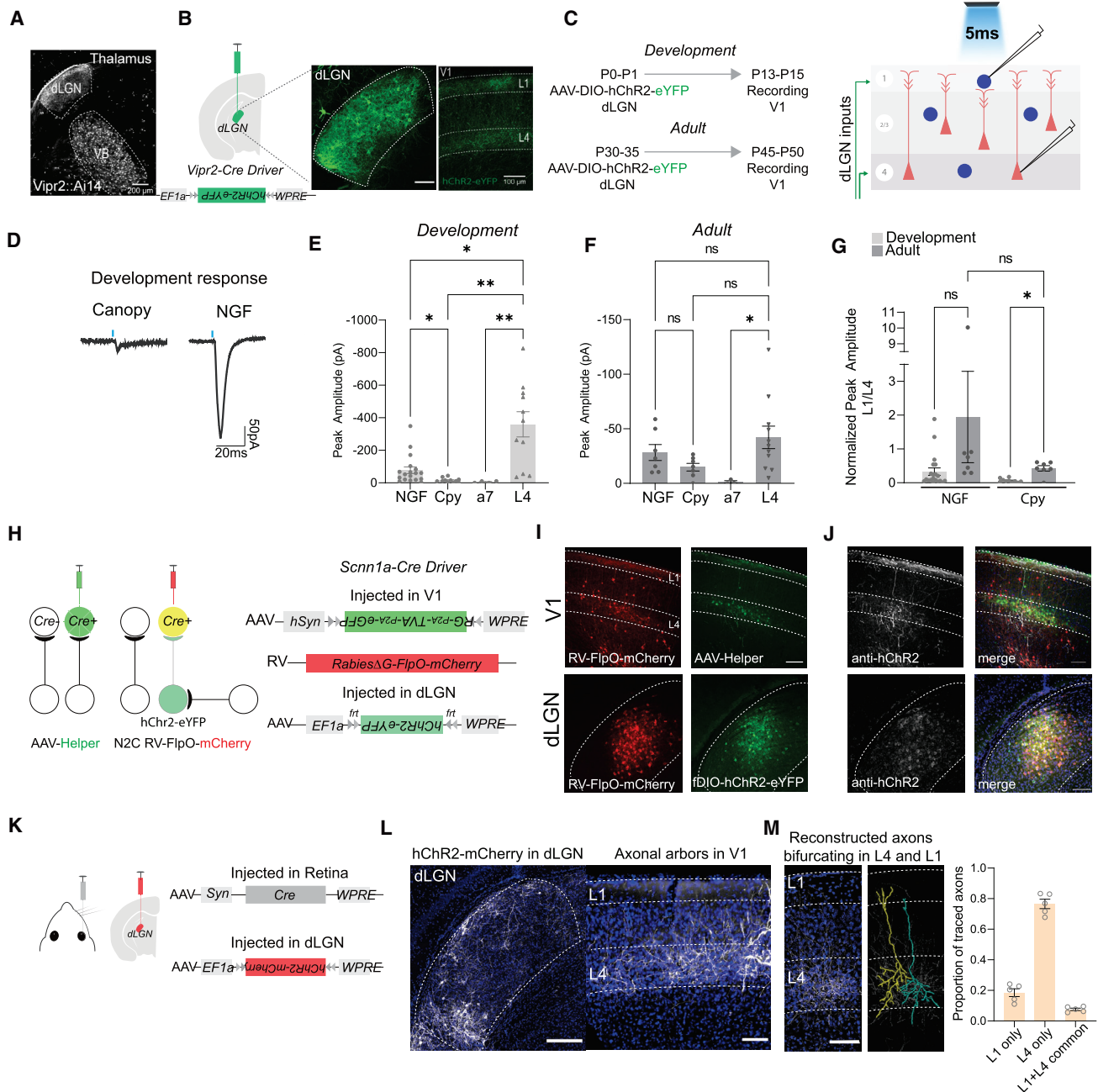


Figure 2. L1 NGF cells and L4 excitatory cells receive dLGN inputs, some of which are shared

(A) Image showing specificity for first-order thalamic nuclei (dLGN and VB), using the *Vipr2-Cre* driver line crossed with the Ai14 reporter line (Cre-dependent tdTomato) at P15. Scale bar, 200 μ m.

(B) Schematic of AAV-DIO-hChr2-eYFP virus injection into the dLGN of the *Vipr2-Cre* driver line (left panel), virus expression in the dLGN (center panel), and resulting axonal projections to L4 and L1 in V1 (right panel). Scale bar, 100 μ m.

(C) Left panel: timeline of AAV-DIO-hChr2-eYFP virus injection (P0–P1, P30–P35) and recording at development time points and adult time points (P13–P15, P45–P50). Right panel: schematic of the slice recording to 5-ms blue light stimulation from L1 INs and L4 excitatory neurons in the same column.

(D) Example excitatory postsynaptic current (EPSC) traces to blue light stimulation of dLGN fibers in V1 L1. Canopy cell response (left panel) and NGF cell response (right panel) from a P14 *Vipr2-Cre* mouse.

(E) Peak EPSC amplitude of all neurons recorded during development (NGF cells $n = 20$; canopy cells $n = 10$; alpha7 cells $n = 4$; L4 cells $n = 10$ from $N = 3$ –4 animals in each condition). One-way ANOVA with Tukey's correction for multiple comparisons; * $p \leq 0.05$; ** $p \leq 0.005$.

(F) Peak EPSC amplitude of all neurons recorded in adults; one-way ANOVA with Tukey's correction for multiple comparisons; * $p \leq 0.05$.

(G) L1 responses normalized to L4 responses in development and adults; one-way ANOVA with Tukey's correction for multiple comparisons; * $p \leq 0.05$.

(legend continued on next page)

Table 1. Key intrinsic physiological properties of NGF and Cpy cells in V1 in development and in the adult

	NGF Development	NGF Adult	Cpy Development	Cpy Adult
Resting membrane potential (mV)	-63.8 ± 0.25	-65.60 ± 1.12	-63.75 ± 0.5	-63.10 ± 0.6
Input resistance (mOhm)	216.794 ± 2.8	282.24 ± 10.77	217.08 ± 4.84	223.01 ± 6.16
Sag voltage deflection (mV)	-2.99 ± 0.07	-4.53 ± 0.26	-4.75 ± 0.24	-3.76 ± 0.301
First spike latency (ms)	529.22 ± 21.7	534.10 ± 54.28	73.56 ± 5.5	69.77 ± 8.99
Rheobase (pA)	124.28 ± 4.04	70.97 ± 6.94	107.5 ± 4.03	86.11 ± 5.32
AP amplitude (mV)	50.67 ± 0.82	53.87 ± 2.18	49.42 ± 1.39	59.24 ± 2.07
AP threshold (mV)	-22.80 ± 0.67	-32.82 ± 1.28	-27.67 ± 0.89	-34.24 ± 0.704
Rise time (ms)	0.485 ± 0.006	0.442 ± 0.02	0.48 ± 0.015	0.417 ± 0.016
Decay time (ms)	1.825 ± 0.025	1.69 ± 0.05	1.68 ± 0.024	1.55 ± 0.07
Half-width (ms)	1.55 ± 0.03	1.41 ± 0.076	1.41 ± 0.039	1.25 ± 0.053
fAHP (mV)	-12.59 ± 0.59	-10.97 ± 1.17	-8.10 ± 0.64	-6.26 ± 0.75
mAHP (mV)	-21.56 ± 0.51	-16.61 ± 0.89	-13.81 ± 0.48	-9.40 ± 0.588

NGF cells are NPY⁺ (Figure S2A), late spiking, and have a ramping-up membrane depolarization with a relatively high rheobase and lower input resistance during development (Figures S2B, left panel, and S2C; see Table 1 for other intrinsic physiological differences between development and adult). Canopy cells, in contrast, are regular spiking, display a small degree of spike adaptation, and have a voltage sag in response to hyperpolarizing current injection (Figure S2B, center panel).

We wanted to determine whether these cell types receive thalamic inputs and, if so, how the strength of these inputs compares with those targeting L4 excitatory cells (the main input thalamo-recipient layer). We found that NGF cells, but not canopy cells, receive considerable direct thalamic input (AMPA current recorded by clamping cells at -70 mV) during development (Figures 2D and 2E; NGF cell response, 97.3 ± 8.8 pA; canopy cell response, 11.63 ± 2.5 pA). Interestingly, in adults, the re-

sponses on canopy cells became comparable with those of NGF cells (Figure 2F). Although, in development and adults, the response of L4 excitatory neurons was, on average, twice that of L1 INs, in some instances, NGF cell responses were comparable (Figure 2G; Takesian et al., 2018). We also performed L1 and L4 recordings in wild-type (WT) mice injected with AAV-hSyn-hChr2-eYFP virus and found that the responses elicited were comparable with those found using the *Vipr2-Cre* line (Figures S3A–S3C). Notably, the largest non NDNF population of L1 INs, alpha-7-expressing L1 INs (Schuman et al., 2019; Figure S2B, right panel), were found to barely receive any thalamic input in development or in the adult (Figures 2E and 2F). Thus, across development, thalamic innervation of L1 INs is cell type specific.

Next we wanted to determine whether the thalamic afferents that project to L1 are shared with those that project to L4. To that end, we utilized a L4-specific *Cre* driver line (*Scnn1a-Cre*) and used a modified rabies approach, where the RV also expresses *FlpO* recombinase together with mCherry. AAV helper and N2c-RV-FlpO-mCherry were co-injected in L4 of V1, followed by an injection of a flp-dependent hChr2-eYFP in the dLGN (Figure 2H). This allowed us to examine the projection pattern of L4-projecting dLGN neurons by using an antibody against hChr2 to visualize the fibers in V1. In addition to their projection in L4, the retrogradely labeled dLGN neurons (Figure 2J, bottom panel) were found to have collaterals in L1 (Figure 2J, top panel). This demonstrates that L4 and L1 share a fraction of inputs from the same thalamic neurons. To independently confirm this, we sparsely labeled neurons in the dLGN by injecting an AAV carrying *Cre* recombinase in the contralateral retina. This virus travels anterogradely and *trans*-synaptically into the dLGN with low efficiency (Zingg et al., 2017). This was followed by an injection of a *Cre*-dependent hChr2-mCherry AAV in the dLGN (Figure 2K) and allowed us to directly visualize dLGN neurons that project to L4 and L1 (Figure 2L). After tracing these axonal arborizations (Figure 2M), we found that there were bifurcating collaterals within L4 and L1 at the single-axon level (Figure 2M, center panel). Those axons that projected to L4 and L1 represented approximately 8% of all axons traced (L1 projecting only, 45 of 224 axons traced; L4 projecting only, 161 of 224; L1 and L4 shared axons, 18 of 224 axons traced) (Figure 2M, right panel). This confirmed that a small subset of thalamic axons targeted both layers, with the majority being either L4 or L1 targeting.

ACC but not RSP inputs to L1 INs strengthen across development

To elucidate the corresponding developmental changes in the strength of top-down inputs, we focused on the projections

(H) Modified FlpO-expressing RV approach to test whether L4 and L1 receive common inputs. *Cre*-dependent AAV-helper and N2c-RV-FlpO-mCherry viruses were injected into V1 of the *Scnn1a-Cre* driver line, followed by flp-dependent AAV-fDIO-hChr2-eYFP virus injection into the dLGN.

(I) Top left panel: N2c-RV-FlpO-mCherry expression in V1. Top right panel: AAV-helper EGFP expression in L4 of V1.

(J) Antibody against hChr2-labeled fibers in V1 (top left panel) and the dLGN (bottom left panel) and merged images from (I) and (J) in V1 (top right panel) and the dLGN (bottom right panel). Scale bar, 100 μm.

(K) Schematic of sparse labeling of neurons in the dLGN. AAV-CamKII-*Cre* virus injected into the right retina results in sparse *trans*-synaptic *Cre* expression in the dLGN, followed by AAV-DIO-hChr2-mCherry virus injection into the dLGN.

(L) Sparse labeling of neurons in the dLGN (left panel; scale bar, 500 μm) and dLGN fibers in V1 (right panel; scale bar, 100 μm).

(M) Left panel: another example image showing labeled axons in L4 and L1. Center panel: NeuroLucida tracing of dLGN axons reveals collaterals in L4 and L1. Right panel: proportion of all traced axons (224 total axons from 5 confocal images across the anterior-posterior axis of V1).

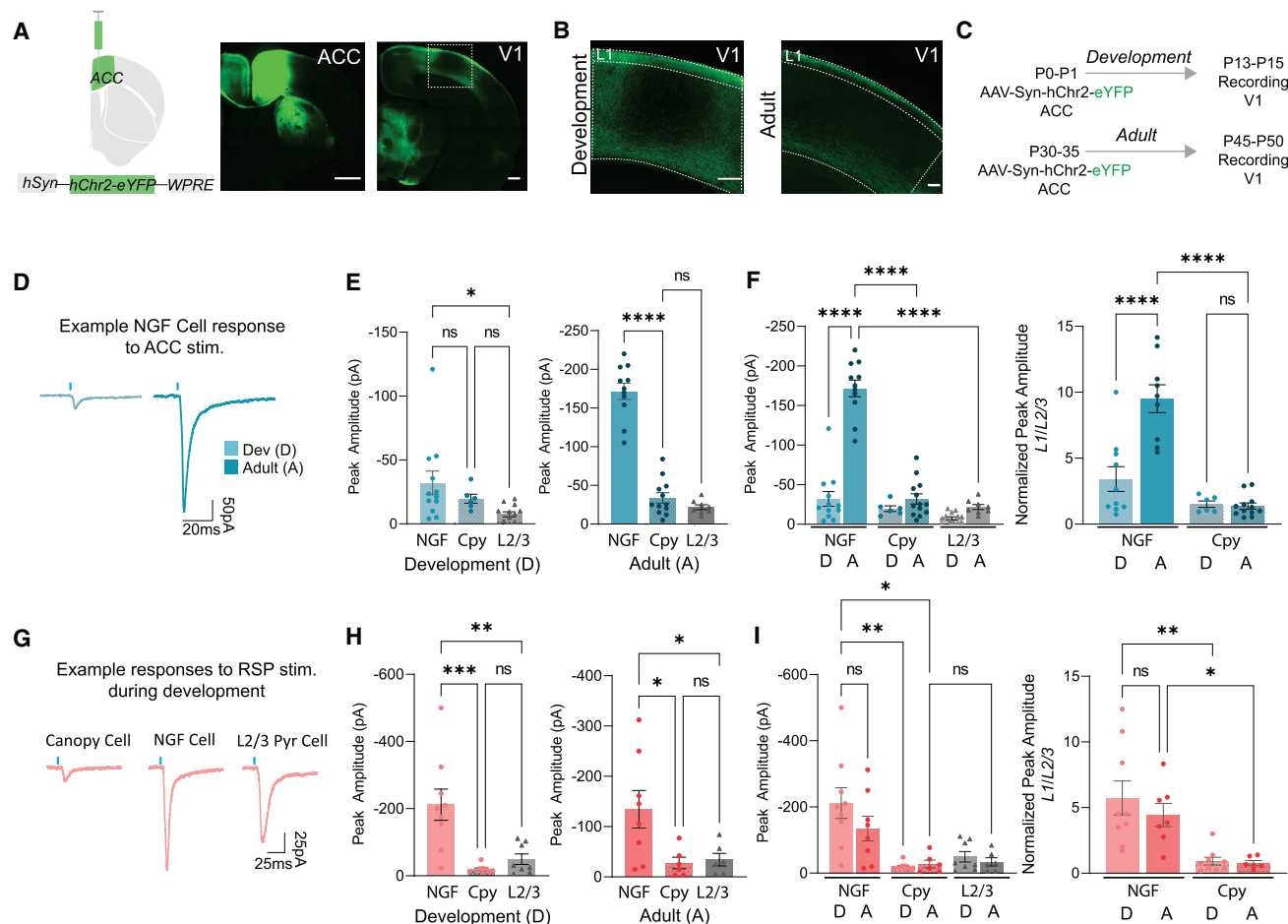


Figure 3. ACC but not RSP inputs to L1 INs strengthen across development

(A) Schematic of hChr2-eYFP virus injection and eYFP expression in the ACC during development (left panel) and its axonal pattern in V1 (right panel). Scale bar, 500 μ m.

(B) Magnified view of the boxed region in (A) (left panel, development) and image of the axonal pattern in the adult V1 (right panel, adult). Scale bar, 100 μ m.

(C) Timeline of virus injection into the ACC and recording in V1 for development and adult time points.

(D) Example traces of a NGF cell in V1 response to optogenetic stimulation of ACC fibers in development (left) and adult (right).

(E) Peak EPSC amplitude (to 5-ms blue light stimulation) of L1 NGF ($n = 12$ cells from $N = 3$ animals) and canopy (Cpy) ($n = 6$ cells from $N = 3$ animals) and L2/3 pyramidal neurons ($n = 13$ cells from $N = 3$ animals) during development (D, left) and in the adult (A, right) (NGF, $n = 11$ cells; Cpy, $n = 12$ cells; L2/3 pyramidal, $n = 8$ cells from $N = 4$ animals). One-way ANOVA with Tukey's correction for multiple comparisons. * $p \leq 0.05$, **** $p \leq 0.001$.

(F) Pairwise comparison of the same data as in (E) in development (D) and adult (A) (left panel) and the same comparison after normalizing to L2/3 pyramidal neurons in the same slice (right); **** $p \leq 0.005$, **** $p \leq 0.001$, unpaired t test.

(G) Example traces of a Cpy, NGF, and L2/3 pyramidal neuron in response to optogenetic stimulation of RSP fibers during D.

(H) Same as in (E) but for RSP stimulation (D, $N = 4$ animals used; NGF: $n = 9$ cells, Cpy: $n = 8$ cells; L2/3: $n = 8$ cells; A, $N = 3$ animals used; NGF: $n = 8$ cells, Cpy $n = 6$ cells, L2/3 $n = 6$ cells). One-way ANOVA with Tukey's correction for multiple comparisons; * $p \leq 0.05$, **** $p \leq 0.005$.

(I) Same as in (F) but for RSP stimulation. One-way ANOVA with Tukey's correction for multiple comparisons; * $p \leq 0.05$, ** $p \leq 0.01$.

from the ACC to V1 because they showed the most dramatic changes across development. In adults, inputs from the ACC have been shown to arborize extensively within L1, targeting various postsynaptic neurons across the different layers of V1 (Leinweber et al., 2017). However, the dynamics by which this input is established across development are unknown. To explore this question, we injected AAV-hSyn-hChr2-eYFP in the ACC region (Figure 3A) and assessed the projection pattern (Figure 3B) and input strength (Figure 3C) in L1 and L2/3 of V1 during development and in the adult. Based on our rabies tracing

results, we expected to see fewer projections from the ACC to V1 during development (Figures 1D and 1E). However, as early as P10, ACC afferents were observed to be distributed across the different layers of V1. Strikingly, these become concentrated within the superficial and deep layers of V1 by adulthood (Figures 3B and S4A). To assess the functional strength of these projections during development (P13–P15) and in the adult (~6–7 weeks), we optogenetically activated the ACC axons in V1 and recorded from the different L1 IN subtypes as well as L2/3 excitatory cells (Figure 3C). To ensure that the observed

differences did not result from differential levels of hChR2 expression, both ages were examined 2 weeks after injection. We found that, during development, despite the abundance of fibers from the ACC to V1 (Figure S4A, right panel), the amplitude of responses in L1 and L2/3 neurons were small (Figures 3D and 3E, left panel; L1 NGF response, -32.075 ± 2.56 pA; L1 canopy response, -19.66 ± 1.314 pA; L2/3 excitatory neuron response, -7.5 ± 0.5 pA). Responses in L1 were still, on average, greater than those observed in L2/3, a trend that becomes more pronounced in the adult (Figure 3E, right panel). Specifically, the peak amplitude of AMPA currents increased by ~ 10 fold in L1 INs by adulthood (Figure 3F). Interestingly, L1 NGF cells were the main recipients of these inputs. Although some of these differences in connectivity strength could be attributed to maturation of their intrinsic properties (Figure S2C; Table 1), the change in current amplitude likely reflects synaptic strengthening. In contrast, the inputs onto alpha-7 (data not shown) and canopy cells were considerably smaller and roughly comparable with those onto L2/3 excitatory cells (Figure 3E; L1 NGF response, -171.6 ± 3.03 pA; L1 canopy response, -38.33 ± 2.179 pA; L2/3 excitatory neuron response, -21.75 ± 1.03 pA). Moreover, other INs in L2/3 also received ACC inputs (Zhang et al., 2014; Ma et al., 2021) but to a lesser degree compared with L1 NGF cells (Figures S4C and S4D; PV response, -4.2 ± 0.32 pA; SST response, -13.8 ± 1.35 pA; VIP response, -18.4 ± 1.76 pA).

Next we wanted to determine whether inputs from the RSP were similarly modulated across development. RSP has been shown to be involved in visual navigation (Makino and Komiyama, 2015; Fischer et al., 2020; Mao et al., 2020), and we found it to be the other major source of cortico-cortical inputs to L1 INs in V1. Given that, compared with the ACC, RSP connectivity is established earlier during development (Figures 1D and 1E), we predicted that it would follow a similar trend but to a lesser degree. Interestingly, although more variable, on average, RSP projections (Figure S4E) remain unchanged across development despite having similar cell type specificity (Figure 3G) in their L1 IN targeting (Figures 3H and 3I; L1 NGF response: -211 ± 14.6 pA [development], -134.5 ± 11 pA [adult]; L1 canopy response: -19.63 ± 1.2 pA [development], -27.58 ± 2.86 pA [adult]; L2/3 excitatory neuron response: -49.5 ± 4.6 pA [development], -34.35 ± 3.12 pA [adult]). These results suggest that the developmental refinement and strengthening of connections from the ACC, but not RSP, to V1 is regulated developmentally and occurs in a progressive and cell-type-specific manner.

L1 NGF cells require bottom-up sensory inputs for strengthening top-down connectivity from the ACC

The observation that bottom-up sensory afferents onto L1 INs are established prior to their receipt of ACC inputs prompted us to ask whether the developmental refinement of these inputs is dependent on sensory activity. To do so, we examined the affect of sensory deprivation on ACC afferent strengthening by performing early postnatal enucleation ($\sim P4$) as well as later, prior to eye opening ($\sim P11$) (Figure 4A). We found that, in the adult V1, enucleation resulted in a significant decrease in the strength of ACC inputs onto L1 NGF cells (Figures 4C–4E; control response, -171.6 ± 3.03 pA; P4-enucleated response,

-33.625 ± 2.36 pA; P11 enucleated response, -20.725 ± 0.95 pA). Interestingly, this did not result in any drastic morphological changes in L1 INs (Figure 4B), but it did result in a small and significant decrease in their input resistance (Figure S5H). In addition, enucleation also results in an increase in the frequency of spontaneous excitatory events onto L1 INs, perhaps as a consequence of a compensatory increase in total excitatory inputs stemming from enucleation (Figures S5A–S5C), as seen in other cell types in the cortex (De Marco García et al., 2015; Franke et al., 2017). Furthermore, when we measured the failure rate of ACC inputs onto L1 NGF cells using a proxy to minimal stimulation (1-ms-long blue light pulse), we observed a significant increase in failed trials in enucleated mice (Figure S5D), suggesting a change in synapse number. Notably, in enucleated animals, a similar reduction was not observed within L2/3 VIP INs, the second largest IN target of ACC inputs in L2/3 of V1 (Figure S5F; control VIP response, -18.4 ± 1.76 pA; enucleated VIP response, -13.3 ± 1.13 pA), suggesting that these INs do not require sensory activity for establishment of their ACC inputs.

Enucleation is also known to have indirect effects on other areas of the visual system (Williams et al., 2002; Nahmani and Turrigiano, 2014; Rose et al., 2016; Jaepel et al., 2017; Bhandari et al., 2020; Hooks and Chen, 2020). Indeed, we observed that this procedure resulted in alteration of the dLGN structure itself (Figure S6A) as well as in the density of thalamic fibers within L1 becoming more diffuse. Moreover, monosynaptic rabies tracing from L1 *NDNF*⁺ INs demonstrated that, although there was no net change in the connectivity from the thalamus, there was a decrease in dLGN connectivity coupled with a corresponding increase in LD and LP afferents (Figure S6C). Using optogenetic stimulation of hChR2-expressing fibers from enucleated (P4 and P11) *Vipr2-Cre* mice, we observed a decrease in dLGN input strength onto L1 NGF cells (Figure S6B). Although the thalamic afferents to L4 excitatory neurons were marginally reduced, their effect on L1 NGF cells was more dramatic. To examine whether a less invasive disruption of sensory input had a similar effect on ACC-to-L1 connectivity, we subjected mice to dark rearing (starting at P4). Similar to enucleation, we observed a decrease in ACC input strength onto NGF cells (Figure 4E) as well as an increase in the failure rate of transmission of these inputs (Figure S5D). Interestingly, enucleation did not result in a change of RSP inputs onto NGF cells in L1 (Figure S5G).

Next, we wanted to confirm whether general sensory activity or direct thalamic inputs to L1 are needed for strengthening of ACC inputs across development. To do so, we injected AAV helpers together with RV-FlpO-mCherry virus into *NDNF-dgCre* pups, followed by an injection of Flp-dependent diphtheria toxin subunit A (DTA) into the dLGN (Figure 4F). This allowed us to selectively ablate only dLGN neurons that innervate L1 INs (Figure 4G), with the caveat that the common inputs between L4 and L1 were also disrupted (which represent only 8% of the thalamic inputs to L4). Importantly, RV-infected L1 INs remain physiologically healthy up to 5 weeks after rabies infection (data not shown; Reardon et al., 2016). Upon reaching adulthood, AAV-hSyn-hChR2-eYFP virus was injected into the ACC, and following a 2-week survival period, RV-injected starter cells were recorded in V1. Similar to what was observed with the

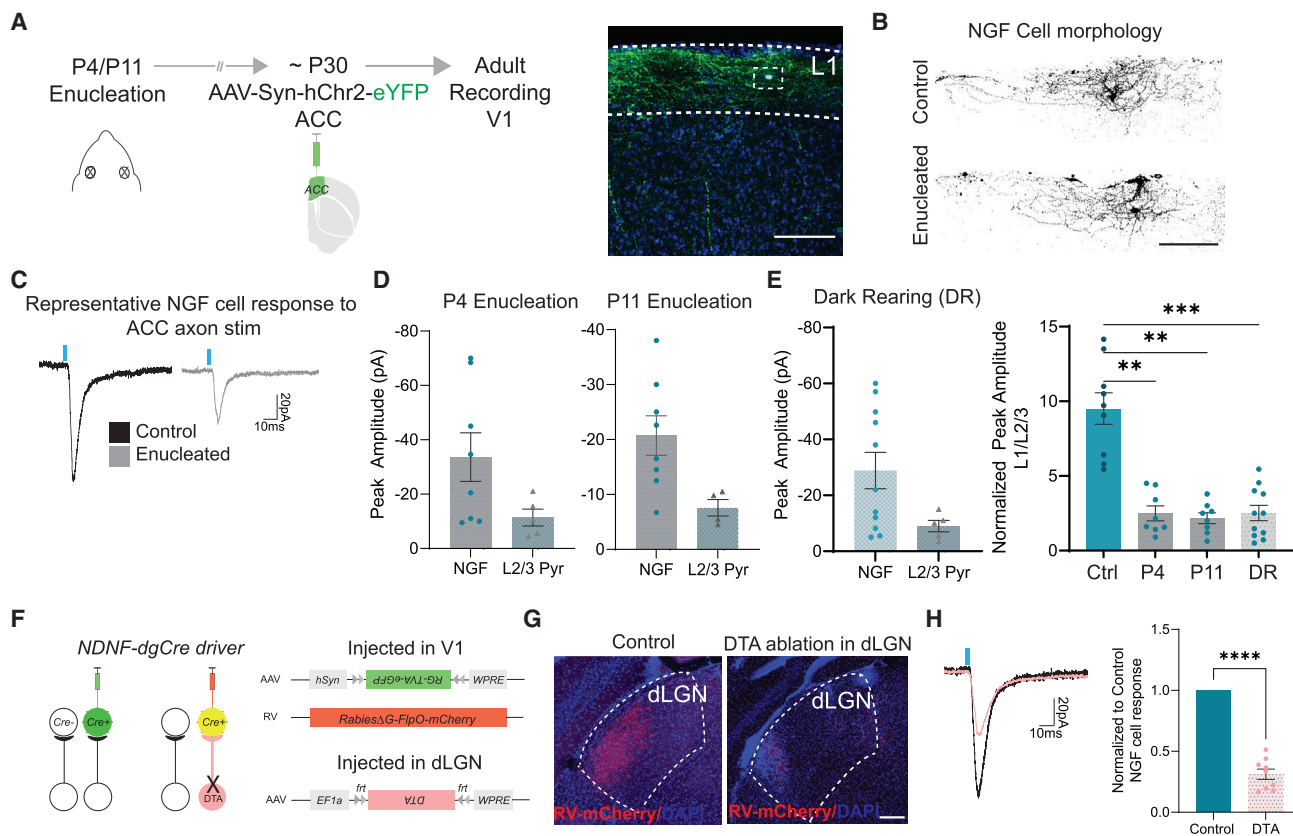


Figure 4. L1 NGF cells require bottom-up sensory inputs for strengthening of top-down connections

(A) Left: timeline of enucleation (P4 or P11), injection of AAV-hChr2 (~P30) into the ACC, and recording in L1 INs in V1 in adults (~P45). Right: example image showing ACC fibers in L1 in P4 enucleated mice. The boxed region shows a filled NGF cell. Scale bar, 100 μ m.

(B) Confocal images of recorded and filled NGF cells in control (above) and P4 enucleated (below) mice. Enucleated cell is shown in the boxed region in (A). Scale bar, 100 μ m.

(C) Example traces of a NGF cell in response to optogenetic stimulation of ACC fibers in control (black) and enucleated (gray) animals.

(D) Comparison of peak amplitude responses (to 5-ms stimulation) of NGF and L2/3 cells under P4 and P11 enucleation conditions to ACC fiber stimulation. Data points represent the number of cells (n) from N = 3–4 animals under each condition.

(E) Left: comparison of peak amplitude responses of NGF and L2/3 cells under dark rearing (DR) conditions. Right: normalized peak amplitudes (to L2/3 pyramidal cells in same slice) for all sensory deprivation conditions. One-way ANOVA with Tukey's correction for multiple comparisons; * $p \leq 0.05$, ** $p \leq 0.01$, *** $p \leq 0.005$.

(F) Schematic of flip-dependent DTA ablation of L1-projecting dLGN axons. Cre-dependent AAV helper and N2C-RV-FlpO-mCherry viruses were injected into V1 of *Ndnf-dgCre* mice; *Flp*-dependent AAV-fDIO-DTA was injected into the dLGN. The timeline for DTA ablations was similar to that in (A) (DTA injection at P4/5, ChR2 injection at P30, recording at ~P45).

(G) Example images showing DTA ablation in the dLGN resulting in elimination of most retrogradely labeled neurons. Scale bar, 200 μ m.

(H) Left: example traces of a NGF cell in V1 response to optogenetic stimulation of ACC fibers in control (black) and DTA-dLGN-ablated afferent (pink) animals. Right: normalized responses of DTA experimental groups compared with WT controls. **** $p \leq 0.0001$, unpaired t test.

sensory deprivation experiments, we found a significant decrease in the strength of ACC inputs onto L1 INs (Figure 4H). Here the response amplitude was normalized to that observed in control non-sensory-deprived animals. These results suggest that bottom-up sensory inputs are required for strengthening of projections from the ACC onto L1 NGF cells in V1.

Top-down connectivity onto L1 NGF cells depends on coordination with bottom-up inputs

Given that compromising bottom-up sensory signaling prevents strengthening of ACC inputs onto L1 NGF cells in V1, we wanted to find out whether early activation of dLGN or ACC inputs would result in premature strengthening of the latter. To explore this

question, in two separate cohorts of pups, we injected the dLGN of *Vipr2-Cre* mice (~P1) with AAV-DIO-hM3D(Gq)-DREADD-mCherry or the ACC with AAV-hM3D(Gq)-DREADD-mCherry (Figures 5A and 5B). In both cases, to measure the strength of top-down inputs, we also injected hChr2-eYFP into the ACC. In the case of ACC-Gq-DREADD activation, we found that at least 70% of ACC neurons expressed mCherry and responded to optogenetic and chemogenetic activation (Figures S7A–S7C).

We then compared the strength of ACC projections onto L1 INs in these two experimental groups at ~P14, following daily injections of clozapine-N-oxide (CNO) or saline (starting at P5; Figure 5C). In comparison with developmental controls (Figure 3E),

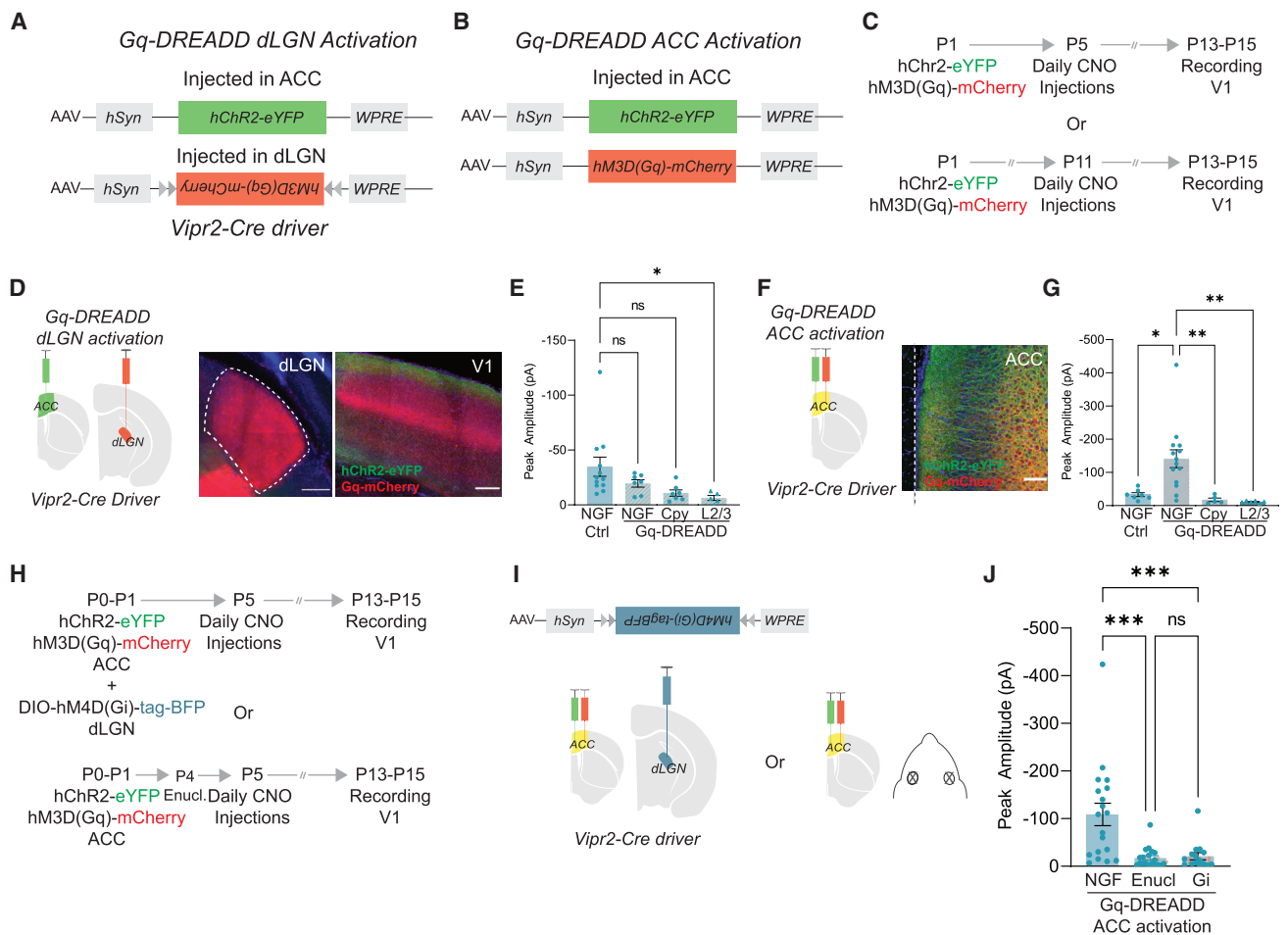


Figure 5. Top-down connectivity onto L1 NGF cells depends on coordination with bottom-up inputs

(A) For Gq-DREADD dLGN activation, AAV-DIO-hM3D(Gq)-DREADD-mCherry was injected into the dLGN, and hChr2-eYFP was injected into the ACC of *Vipr2-Cre* mice.
 (B) For Gq-DREADD ACC activation, AAV-hM3D(Gq)-DREADD-mCherry and hChr2 eYFP were co-injected into the ACC of *Vipr2-Cre* mice.
 (C) Timeline of AAV virus injection (P1), CNO administration (daily, starting at P5), and recording of L1 INs in V1 (~P13–P15).
 (D) Schematic of the Gq-DREADD dLGN activation experiment (left panel), expression of Gq-DREADD-mCherry in the thalamus (center panel), and co-expression of Gq-DREADD-mCherry in the dLGN and hChr2-eYFP axons in V1 (right panel). Scale bar, 200 μ m.
 (E) Comparison of peak EPSC amplitude response of the different cell types in V1 to ACC hChr2 stimulation: control versus Gq-DREADD dLGN activation. NGF, neurogliaform. Here the developmental control is same as in Figure 3E. One-way ANOVA with Tukey's correction for multiple comparisons; NS \geq 0.05, * $p \leq$ 0.05
 (F) Schematic of the Gq-DREADD ACC activation experiment (left panel) and co-expression of Gq-DREADD-mCherry and hChr2-eYFP in the ACC (right panel). Scale bar, 100 μ m.
 (G) Same as (E) but in CNO-only control versus Gq-DREADD ACC activation. One-way ANOVA with Tukey's correction for multiple comparisons; * $p \leq$ 0.05; ** $p \leq$ 0.01; NS comparisons not shown.
 (H) Timeline of AAV virus injections (P1), CNO administration (daily, starting at P5) and recording in L1 INs in V1 (~P13–P15, top panel) or enucleation timeline (bottom panel).
 (I) Schematic of the AAV-DIO-hM4D(Gi)-DREADD-tBFP dLGN inhibition experiment with simultaneous activation of the ACC with Gq-DREADD (left panel) and schematic of enucleation combined with activation of the ACC with Gq DREADD (right panels). In both experiments, the ACC was injected with AAV-hChr2 as in (E) and (F).
 (J) Comparison of the peak amplitude response of L1 NGF cells to hChr2 stimulation: Gq-DREADD ACC activation conditions (the same as in Figure 5G) versus Gq-DREADD ACC activation + enucleation conditions (Enucl, center bar), and Gq-DREADD ACC activation + Gi-DREADD dLGN inhibition conditions (Gi, right bar). One-way ANOVA with Tukey's correction for multiple comparisons; *** $p \leq$ 0.005.

we did not observe strengthening of ACC projections onto L1 INs when the dLGN pathway was overactivated (Figures 5D and 5E). In contrast, selective activation of the ACC pathway (CNO starting at P5 or P11) resulted in a significant increase in ACC input strength onto L1 INs cells compared with saline- or CNO-injected

control groups (Figures 5F, 5G, and S7D). Moreover, this increase was specific to the NGF cell population and was not observed in canopy, a7, or L2/3 excitatory neurons (saline control response: -34.38 ± 3.72 pA, CNO control response: -42.81 ± 2.94 pA versus Gq-DREADD-ACC [CNO starting at P5] NGF cell

response: -163.529 ± 6.84 pA, Gq-DREADD-ACC [CNO starting at P11] NGF cell response: -164.22 ± 9.55 pA; Gq-DREADD-ACC canopy cell response: -17.4 ± 2.08 pA, Gq-DREADD-ACC L2/3 response: -11.4 ± 0.55 pA). On average, there was a ~4-fold increase in the strength of ACC inputs to NGF cells following ACC-Gq-DREADD activation. This was coupled with a decrease in the percentage of failed trials in response to a 1-ms blue light pulse (~32.5% in saline/CNO control versus ~12% in Gq-DREADD ACC-activated mice) (Figure S7E). Although the premature increase in strength could be attributed to a general plasticity mechanism, the cell type specificity of this increase was very striking.

We wanted to find out whether this augmentation of the strength of ACC afferents to L1 NGF cells was dependent on bottom-up sensory thalamic signals. We reasoned that this may occur because of the coordinated engagement of bottom-up and ACC afferents converging onto L1 NGF cells (Figure 4). We therefore hypothesized that this augmentation should be dependent on bottom-up sensory activity and that dampening of sensory signaling would impair this phenomenon. To achieve this, we injected AAV-DIO-hM4D(Gi)-DREADD-tBFP into the dLGN (in *Vipr2-Cre* pups) or enucleated the mice at P4 while expressing Gq-DREADD and hChR2 in the ACC and similarly performed whole-cell recording at P13–P15 (Figures 5H and 5I). Consistent with our hypothesis, both manipulations reversed the ability of Gq-DREADD activation of the ACC to increase the synaptic strength of ACC afferents onto L1 NGF cells (Figure 5J).

Next we queried whether there exists a threshold requirement for bottom-up activity or whether enhanced co-activation of ACC and dLGN afferents would further increase the strength of the ACC inputs. To explore this, we injected the dLGN of *Vipr2-Cre* pups (~P1) and the ACC with a HM3D(Gq)-DREADD-mCherry-expressing AAV and, as in earlier experiments, co-injected hChR2-eYFP into the ACC (Figure S7F, left panel). As expected, upon CNO administration, the strength of ACC afferents was increased (Figure S7F, right panel). However, this did not increase the strength of the ACC afferents beyond what we observed when we activated them in the absence of enhanced dLGN activation (Figure S7G). We concluded that, although activity of the dLGN is required for enhancement of ACC connectivity, additional activation of the dLGN does not result in further strengthening of ACC afferents.

DISCUSSION

INs in the superficial visual cortex have been shown to receive bottom-up sensory inputs and top-down corticocortical afferents from the ACC. Despite the prevalence of ACC fibers in L1 of V1, previous studies have not explored the extent to which INs in this layer receive these inputs. Here we observe that among L1 INs, NGF cells notably receive ACC as well as bottom-up sensory afferents. In addition, we demonstrate that a small portion of dLGN afferents to L1 are shared with those in L4. Furthermore, we find that, during development, strengthening of ACC afferents onto L1 NGF cells requires earlier receipt of thalamic inputs from the dLGN. By exploring the role of coordinated activity between ACC and thalamic fibers, we find that chemogenetic activation of the ACC can modulate the strength

of these top-down inputs. In contrast, although thalamic afferents are necessary for acquisition of ACC inputs to NGF cells, a threshold level of activity was sufficient.

L1 NGF cells receive early thalamic inputs

In our rabies tracing of L1 INs in V1, we observed that thalamic afferents originate from the dLGN as well as the higher-order LP thalamus. While the dLGN is thought to primarily convey sensory signals, the LP receives input from a variety of sources, including the superior colliculus (Gale and Murphy, 2014; Fang et al., 2020) as well as cortical feedback (Bennett et al., 2019). This suggests that the activity in the LP reflects higher-order signaling from a variety of modalities in addition to visual inputs. How these two sources of thalamic input are coordinated within L1 INs is poorly understood. Recent work has implicated LP activity playing a role to suppress noise in the visual cortex through a L1 mechanism (Fang et al., 2020). However, the specific INs within L1 that mediate this signaling remain unknown. Despite the presence of first- and higher-order thalamic inputs to NDNF+ L1 INs, our findings indicate that, in this layer, these INs are innervated more abundantly by the dLGN. Interestingly, this trend shifts in enucleated mice, where the size of LP and LD inputs becomes equivalent to those from the dLGN.

Previous studies from our laboratory and others have demonstrated that superficial NGF cells receive thalamic inputs at early postnatal ages (De Marco García et al., 2015; Che et al., 2018). Despite their positioning in the superficial cortex, by P15 NGF cells receive bottom-up activity. They perhaps receive these afferents as early as the SST INs in deep layers, the latter of which are the first-born IN population (Marques-Smith et al., 2016; Tuncdemir et al., 2016; Pouchelon et al., 2020). Given that first-order thalamic inputs are present in L4 and L1 in V1, it is appealing to consider whether coordinated induction of excitation within L4 and inhibition within L1 may have developmental functional significance. Despite the considerable strength of dLGN inputs onto L1 NGF cells, our preliminary examination of their output during development (data not shown) suggests that these connections may not produce strong inhibition. Instead, our results indicate that the sensory thalamic inputs to L1 NGF cells are essential for promotion of afferent connectivity from the ACC, perhaps through a coincident depolarization and Hebbian mechanism, increasing synapse number and strength. Interestingly, previous work from our group indicates that early thalamic inputs to S1 function competitively with local excitatory inputs to NGF cells (De Marco García et al., 2015). Specifically, when NMDA signaling is ablated, it results in a shift in the connectivity of these cells from receiving thalamic to receiving local cortical afferents. Notably, this study focused on L2/3 NGF cells rather than those in L1. Our present work reveals that thalamic afferents onto L1 NGF cells in the visual cortex cooperate with long-range inputs from the ACC, resulting in their developmental strengthening. Taken together, these results indicate that local and long-range connectivity onto L1 NGF cells are centrally dependent on early thalamic afferents.

L1 NGF cells function in coordination of bottom-up and top-down signaling

While L1 INs have been previously shown to receive bottom-up sensory inputs (Ji et al., 2016), we demonstrate that this is

specific to the NGF cell population during development. In addition, the dLGN afferents to L1 NGF cells at least in part represent efferent copy of the sensory afferents to the L4 cells. This suggests that NGF cells in L1 are uniquely positioned to coordinate the activity of bottom-up and top-down signaling in the superficial layers of the visual cortex. It is likely that thalamic first-order afferents to NGF cells synergize with projections from other sources. Although previous studies implicate that cholinergic afferents may subserve this role (Letzkus et al., 2011; Alitto and Dan, 2013; Fan et al., 2020), our work implicates co-recruitment of ACC afferents as a potential source of their engagement.

L1 NGF cells have late-spiking properties and are thought to signal through volume transmission, which provides strong and sustained inhibition in the superficial visual cortex. This positions them to function in suppressing activity when bottom-up and top-down signals are coordinated. This could potentially be useful in contexts where the expected internal representation is in concordance with bottom-up sensory signals. They therefore could be functioning in a manner akin to what has been proposed for PV INs, which have been implicated in suppression of self-generated movements in the auditory cortex (Schneider et al., 2018). In a complementary fashion to L1 NGF cells, VIP INs in L2/3 also receive top-down signals, including from the ACC (Zhang et al., 2014), but, notably, not direct bottom-up inputs (Ji et al., 2016). VIP INs disinhibit SST INs (Lee et al., 2013; Fu et al., 2014), the latter of which has been shown to be activated during visual learning (Attinger et al., 2017). Our results indicate that ACC connectivity onto VIP INs is not altered with sensory deprivation, suggesting a role of bottom-up inputs in strengthening of ACC afferents specifically onto L1 NGF cells. Interestingly, RSP inputs onto L1 NGF cells were also not altered significantly in enucleated mice. In part, this was expected based on the lack of developmental modulation of these inputs onto L1 NGF cells. But it was also surprising because it could be expected that navigation-based top-down circuitry requires sensory inputs/experience. Based on our results, it is likely that these connections are hardwired and minimally altered across development/sensory manipulations or that other inputs are more important in establishment of RSP connectivity.

Thus, emerging evidence has begun to reveal how different IN populations are coordinated to support cortical computations. Our findings provide insight into the contexts in which L1 NGF cells are likely recruited. Interestingly, we observed that the NGF cells in the auditory cortex are organized similarly as those we report here (data not shown). Future experiments will reveal how these populations are engaged *in vivo* in auditory and visual tasks and how the balance between bottom-up and top-down circuit development is disrupted in neurodevelopmental and neuropsychiatric disorders.

STAR★METHODS

Detailed methods are provided in the online version of this paper and include the following:

- KEY RESOURCES TABLE
- RESOURCE AVAILABILITY
 - Lead contact

- Materials availability
- Data and code availability
- EXPERIMENTAL MODEL AND SUBJECT DETAILS
 - Mice
- METHOD DETAILS
 - Sensory deprivations
 - Histology
 - Rabies tracing
 - Viruses
 - *Trans*-synaptic labeling
 - Image analysis
 - Stereotaxic Injections for optogenetics and slice recording
 - *In vitro* electrophysiology
 - CNO injections
 - NeuroLucida tracing
- QUANTIFICATION AND STATISTICAL ANALYSIS

SUPPLEMENTAL INFORMATION

Supplemental information can be found online at <https://doi.org/10.1016/j.neuron.2021.08.004>.

ACKNOWLEDGMENTS

We thank Dr. Anne Takesian and Dr. Chinfai Chen for their valuable comments on the manuscript. We also thank Dr. Shruti Muralidhar for proofreading the manuscript. We thank Dr. Tim Burbridge for demonstrating retinal injections. This work was supported by a Goldenson Foundation grant (FY18) and a Hearst Foundation grant (FY19) (to L.A.I.), grants from the National Institutes of Health (NIH) (MH071679, NS08297, NS074972, and MH095147 to G.F. and P01NS074972, R01NS107257, and R01NS110079 to B.R.), as well as support from the Simons Foundation (SFARI to G.F.).

AUTHOR CONTRIBUTIONS

L.A.I. and G.F. conceived the project and wrote the manuscript. L.A.I. performed experiments and analyses. S.H. carried out dLGN injections, recording, and analyses. M.F.-O., Y.Q., and S.V. assisted with histology experiments. M.S., Y.Q., and S.V. assisted with tiling scope imaging and rabies quantification. M.S. assisted with NeuroLucida reconstructions. Q.X. produced some of the viruses used in the study (labeled NYUAD). G.P. contributed to design and cloning of VTK constructs and AAV helper. R.M. and B.R. contributed to the design of the experiments and discussions.

DECLARATION OF INTERESTS

G.F. is a founder of Regel.

INCLUSION AND DIVERSITY

One or more of the authors of this paper self-identifies as an underrepresented ethnic minority in science. One or more of the authors of this paper self-identifies as a member of the LGBTQ+ community. One or more of the authors of this paper self-identifies as living with a disability. While citing references scientifically relevant for this work, we also actively worked to promote gender balance in our reference list.

Received: February 9, 2021

Revised: July 8, 2021

Accepted: August 6, 2021

Published: September 2, 2021

REFERENCES

- Abs, E., Poorthuis, R.B., Apelblat, D., Muhammad, K., Pardi, M.B., Enke, L., Kushinsky, D., Pu, D.L., Eizinger, M.F., Conzelmann, K.K., et al. (2018). Learning-Related Plasticity in Dendrite-Targeting Layer 1 Interneurons. *Neuron* *100*, 684–699.e6.
- Allitto, H.J., and Dan, Y. (2013). Cell-type-specific modulation of neocortical activity by basal forebrain input. *Front. Syst. Neurosci.* *6*, 79.
- Anastasiades, P.G., Collins, D.P., and Carter, A.G. (2020). Mediodorsal and Ventromedial Thalamus Engage Distinct L1 Circuits in the Prefrontal Cortex. *Neuron* *109*, 314–330.e4.
- Ardid, S., Wang, X.J., and Compte, A. (2007). An integrated microcircuit model of attentional processing in the neocortex. *J. Neurosci.* *27*, 8486–8495.
- Attinger, A., Wang, B., and Keller, G.B. (2017). Visuomotor Coupling Shapes the Functional Development of Mouse Visual Cortex. *Cell* *169*, 1291–1302.e14.
- Bennett, C., Gale, S.D., Garrett, M.E., Newton, M.L., Callaway, E.M., Murphy, G.J., and Olsen, S.R. (2019). Higher-Order Thalamic Circuits Channel Parallel Streams of Visual Information in Mice. *Neuron* *102*, 477–492.e5.
- Bhandari, A., Smith, J., and Van Hook, M.J. (2020). Bilateral enucleation induces homeostatic plasticity in the dorsolateral geniculate nucleus of mice. *bioRxiv*. <https://doi.org/10.1101/2020.11.02.365130>.
- Boyden, E.S., Zhang, F., Bamberg, E., Nagel, G., and Deisseroth, K. (2005). Millisecond-timescale, genetically targeted optical control of neural activity. *Nat. Neurosci.* *8*, 1263–1268.
- Che, A., Babji, R., Iannone, A.F., Fetcho, R.N., Ferrer, M., Liston, C., Fishell, G., and De Marco García, N.V. (2018). Layer I Interneurons Sharpen Sensory Maps during Neonatal Development. *Neuron* *99*, 98–116.e7.
- Chou, S.J., Babot, Z., Leingärtner, A., Studer, M., Nakagawa, Y., and O’Leary, D.D. (2013). Geniculocortical input drives genetic distinctions between primary and higher-order visual areas. *Science* *340*, 1239–1242.
- Cohen-Kashi Malina, K., Tsvourakis, E., Kushinsky, D., Apelblat, D., Shtiglitz, S., Zohar, E., Sokoletsy, M., Tasaka, G.I., Mizrahi, A., Lampl, I., and Spiegel, I. (2021). NDNF interneurons in layer 1 gain-modulate whole cortical columns according to an animal’s behavioral state. *Neuron* *109*, 2150–2164.e5.
- Colonnese, M.T., Kaminska, A., Minlebaev, M., Milh, M., Bloem, B., Lescuré, S., Moriette, G., Chiron, C., Ben-Ari, Y., and Khazipov, R. (2010). A conserved switch in sensory processing prepares developing neocortex for vision. *Neuron* *67*, 480–498.
- Cruikshank, S.J., Ahmed, O.J., Stevens, T.R., Patrick, S.L., Gonzalez, A.N., Elmaleh, M., and Connors, B.W. (2012). Thalamic control of layer 1 circuits in prefrontal cortex. *J. Neurosci.* *32*, 17813–17823.
- De Marco García, N.V., Priya, R., Tuncdemir, S.N., Fishell, G., and Karayannis, T. (2015). Sensory inputs control the integration of neurogliaform interneurons into cortical circuits. *Nat. Neurosci.* *18*, 393–401.
- Desimone, R., and Duncan, J. (1995). Neural mechanisms of selective visual attention. *Annu. Rev. Neurosci.* *18*, 193–222.
- Dominguez, S., Ma, L., Yu, H., Pouchelon, G., Mayer, C., Spyropoulos, G.D., Cea, C., Buzsáki, G., Fishell, G., Khodagholy, D., and Gelinias, J.N. (2021). A transient postnatal quiescent period precedes emergence of mature cortical dynamics. *eLife* *10*, e69011.
- Fan, L.Z., Kheifets, S., Böhm, U.L., Wu, H., Piatkevich, K.D., Xie, M.E., Parot, V., Ha, Y., Evans, K.E., Boyden, E.S., et al. (2020). All-Optical Electrophysiology Reveals the Role of Lateral Inhibition in Sensory Processing in Cortical Layer 1. *Cell* *180*, 521–535.e18.
- Fang, Q., Chou, X.L., Peng, B., Zhong, W., Zhang, L.I., and Tao, H.W. (2020). A Differential Circuit via Retino-Colliculo-Pulvinar Pathway Enhances Feature Selectivity in Visual Cortex through Surround Suppression. *Neuron* *105*, 355–369.e6.
- Fenno, L.E., Mattis, J., Ramakrishnan, C., Hyun, M., Lee, S.Y., He, M., Tucciarone, J., Selimbeyoglu, A., Berndt, A., Grosenick, L., et al. (2014). Targeting cells with single vectors using multiple-feature Boolean logic. *Nat. Methods* *11*, 763–772.
- Fischer, L.F., Mojica Soto-Albors, R., Buck, F., and Harnett, M.T. (2020). Representation of visual landmarks in retrosplenial cortex. *eLife* *9*, e51458.
- Frangeul, L., Kehayas, V., Sanchez-Mut, J.V., Fièvre, S., Krishna-K, K., Pouchelon, G., Telley, L., Bellone, C., Holtmaat, A., Gräff, J., et al. (2017). Input-dependent regulation of excitability controls dendritic maturation in somatosensory thalamocortical neurons. *Nat. Commun.* *8*, 2015.
- Fu, Y., Tucciarone, J.M., Espinosa, J.S., Sheng, N., Darcy, D.P., Nicoll, R.A., Huang, Z.J., and Stryker, M.P. (2014). A cortical circuit for gain control by behavioral state. *Cell* *156*, 1139–1152.
- Gale, S.D., and Murphy, G.J. (2014). Distinct representation and distribution of visual information by specific cell types in mouse superficial superior colliculus. *J. Neurosci.* *34*, 13458–13471.
- Hooks, B.M., and Chen, C. (2020). Circuitry Underlying Experience-Dependent Plasticity in the Mouse Visual System. *Neuron* *106*, 21–36.
- Huda, R., Sipe, G.O., Breton-Provencher, V., Cruz, K.G., Pho, G.N., Adam, E., Gunter, L.M., Sullins, A., Wickersham, I.R., and Sur, M. (2020). Distinct prefrontal top-down circuits differentially modulate sensorimotor behavior. *Nat. Commun.* *11*, 6007.
- Ibrahim, L.A., Mesik, L., Ji, X.Y., Fang, Q., Li, H.F., Li, Y.T., Zingg, B., Zhang, L.I., and Tao, H.W. (2016). Cross-Modality Sharpening of Visual Cortical Processing through Layer-1-Mediated Inhibition and Disinhibition. *Neuron* *89*, 1031–1045.
- Ibrahim, L.A., Schuman, B., Bandler, R., Rudy, B., and Fishell, G. (2020). Mining the jewels of the cortex’s crowning mystery. *Curr. Opin. Neurobiol.* *63*, 154–161.
- Jaepel, J., Hübener, M., Bonhoeffer, T., and Rose, T. (2017). Lateral geniculate neurons projecting to primary visual cortex show ocular dominance plasticity in adult mice. *Nat. Neurosci.* *20*, 1708–1714.
- Ji, X.Y., Zingg, B., Mesik, L., Xiao, Z., Zhang, L.I., and Tao, H.W. (2016). Thalamocortical Innervation Pattern in Mouse Auditory and Visual Cortex: Laminar and Cell-Type Specificity. *Cereb. Cortex* *26*, 2612–2625.
- Jiang, X., Wang, G., Lee, A.J., Stornetta, R.L., and Zhu, J.J. (2013). The organization of two new cortical interneuronal circuits. *Nat. Neurosci.* *16*, 210–218.
- Kastner, S., and Ungerleider, L.G. (2000). Mechanisms of visual attention in the human cortex. *Annu. Rev. Neurosci.* *23*, 315–341.
- Kawaguchi, Y., and Kubota, Y. (1997). GABAergic cell subtypes and their synaptic connections in rat frontal cortex. *Cereb. Cortex* *7*, 476–486.
- Krashes, M.J., Koda, S., Ye, C., Rogan, S.C., Adams, A.C., Cusher, D.S., Maratos-Flier, E., Roth, B.L., and Lowell, B.B. (2011). Rapid, reversible activation of AgRP neurons drives feeding behavior in mice. *J. Clin. Invest.* *121*, 1424–1428.
- Lee, S., Kruglikov, I., Huang, Z.J., Fishell, G., and Rudy, B. (2013). A disinhibitory circuit mediates motor integration in the somatosensory cortex. *Nat. Neurosci.* *16*, 1662–1670.
- Lee, A.J., Wang, G., Jiang, X., Johnson, S.M., Hoang, E.T., Lanté, F., Stornetta, R.L., Beenhakker, M.P., Shen, Y., and Julius Zhu, J. (2015). Canonical Organization of Layer 1 Neuron-Led Cortical Inhibitory and Disinhibitory Interneuronal Circuits. *Cereb. Cortex* *25*, 2114–2126.
- Leinweber, M., Ward, D.R., Sobczak, J.M., Attinger, A., and Keller, G.B. (2017). A Sensorimotor Circuit in Mouse Cortex for Visual Flow Predictions. *Neuron* *96*, 1204.
- Letzkus, J.J., Wolff, S.B., Meyer, E.M., Tovote, P., Courtin, J., Herry, C., and Lüthi, A. (2011). A disinhibitory microcircuit for associative fear learning in the auditory cortex. *Nature* *480*, 331–335.
- Luhmann, H.J., and Khazipov, R. (2018). Neuronal activity patterns in the developing barrel cortex. *Neuroscience* *368*, 256–267.
- Ma, G., Liu, Y., Wang, L., Xiao, Z., Song, K., Wang, Y., Peng, W., Liu, X., Wang, Z., Jin, S., et al. (2021). Hierarchy in sensory processing reflected by innervation balance on cortical interneurons. *Sci. Adv.* *7*, eabf5676.
- Makino, H., and Komiyama, T. (2015). Learning enhances the relative impact of top-down processing in the visual cortex. *Nat. Neurosci.* *18*, 1116–1122.

- Mao, D., Molina, L.A., Bonin, V., and McNaughton, B.L. (2020). Vision and Locomotion Combine to Drive Path Integration Sequences in Mouse Retrosplenial Cortex. *Curr. Biol.* *30*, 1680–1688.e4.
- Marques-Smith, A., Lyngholm, D., Kaufmann, A.K., Stacey, J.A., Hoerder-Suabedissen, A., Becker, E.B., Wilson, M.C., Molnár, Z., and Butt, S.J. (2016). A Transient Translaminar GABAergic Interneuron Circuit Connects Thalamocortical Recipient Layers in Neonatal Somatosensory Cortex. *Neuron* *89*, 536–549.
- Meng, X., Xu, Y., Kao, J.P.Y., and Kanold, P.O. (2020). Transient coupling between subplate and subgranular layers to L1 neurons before and during the critical period. *bioRxiv*. <https://doi.org/10.1101/2020.05.05.077784>.
- Mesik, L., Huang, J.J., Zhang, L.I., and Tao, H.W. (2019). Sensory- and motor-related responses of layer 1 neurons in the mouse visual cortex. *J. Neurosci.* *39*, 10060–10070.
- Muralidhar, S., Wang, Y., and Markram, H. (2014). Synaptic and cellular organization of layer 1 of the developing rat somatosensory cortex. *Front. Neuroanat.* *7*, 52.
- Nahmani, M., and Turrigiano, G.G. (2014). Deprivation-induced strengthening of presynaptic and postsynaptic inhibitory transmission in layer 4 of visual cortex during the critical period. *J. Neurosci.* *34*, 2571–2582.
- Naskar, S., Qi, J., Pereira, F., Gerfen, C.R., and Lee, S. (2021). Cell-type-specific recruitment of GABAergic interneurons in the primary somatosensory cortex by long-range inputs. *Cell Rep.* *34*, 108774.
- Nassi, J.J., and Callaway, E.M. (2009). Parallel processing strategies of the primate visual system. *Nat. Rev. Neurosci.* *10*, 360–372.
- Oh, S.W., Harris, J.A., Ng, L., Winslow, B., Cain, N., Mihalas, S., Wang, Q., Lau, C., Kuan, L., Henry, A.M., et al. (2014). A mesoscale connectome of the mouse brain. *Nature* *508*, 207–214.
- Palmer, L.M., Schulz, J.M., Murphy, S.C., Ledergerber, D., Murayama, M., and Larkum, M.E. (2012). The cellular basis of GABA(B)-mediated interhemispheric inhibition. *Science* *335*, 989–993.
- Pardi, M.B., Vogenstahl, J., Dalmay, T., Spanò, T., Pu, D.L., Naumann, L.B., Kretschmer, F., Sprekeler, H., and Letzkus, J.J. (2020). A thalamocortical top-down circuit for associative memory. *Science* *370*, 844–848.
- Pouchelon, G., Gambino, F., Bellone, C., Telley, L., Vitali, I., Lüscher, C., Holtmaat, A., and Jabaudon, D. (2014). Modality-specific thalamocortical inputs instruct the identity of postsynaptic L4 neurons. *Nature* *511*, 471–474.
- Pouchelon, G., Bollman, Y., Fisher, E., Agba, C.K., Xu, Q., Ritola, K.D., Mirow, A.M.C., Kim, S., Cossart, R., and Fishell, G. (2020). The organization and developmental establishment of cortical interneuron presynaptic circuits. *bioRxiv*. <https://doi.org/10.1101/2020.09.17.302117>.
- Rao, R.P., and Ballard, D.H. (1999). Predictive coding in the visual cortex: a functional interpretation of some extra-classical receptive-field effects. *Nat. Neurosci.* *2*, 79–87.
- Reardon, T.R., Murray, A.J., Turi, G.F., Wirblich, C., Croce, K.R., Schnell, M.J., Jessell, T.M., and Losonczy, A. (2016). Rabies Virus CVS-N2c(ΔG) Strain Enhances Retrograde Synaptic Transfer and Neuronal Viability. *Neuron* *89*, 711–724.
- Rose, T., Jaepel, J., Hübener, M., and Bonhoeffer, T. (2016). Cell-specific restoration of stimulus preference after monocular deprivation in the visual cortex. *Science* *352*, 1319–1322.
- Roth, M.M., Dahmen, J.C., Muir, D.R., Imhof, F., Martini, F.J., and Hofer, S.B. (2016). Thalamic nuclei convey diverse contextual information to layer 1 of visual cortex. *Nat. Neurosci.* *19*, 299–307.
- Saalman, Y.B., Pinsk, M.A., Wang, L., Li, X., and Kastner, S. (2012). The pulvinar regulates information transmission between cortical areas based on attention demands. *Science* *337*, 753–756.
- Schneider, D.M., Sundararajan, J., and Mooney, R. (2018). A cortical filter that learns to suppress the acoustic consequences of movement. *Nature* *561*, 391–395.
- Schuman, B., Machold, R., Hashikawa, Y., Fuzik, J., Fishell, G., and Rudy, B. (2018). Four unique interneuron populations reside in neocortical layer 1. *J. Neurosci.* *39*, 125–139.
- Schuman, B., Machold, R.P., Hashikawa, Y., Fuzik, J., Fishell, G.J., and Rudy, B. (2019). Four Unique Interneuron Populations Reside in Neocortical Layer 1. *J. Neurosci.* *39*, 125–139.
- Schuman, B., Dellal, S., Prönneke, A., Machold, R., and Rudy, B. (2021). Neocortical Layer 1: An Elegant Solution to Top-Down and Bottom-Up Integration. *Annu. Rev. Neurosci.* *44*, 221–252.
- Squire, R.F., Noudoost, B., Schafer, R.J., and Moore, T. (2013). Prefrontal contributions to visual selective attention. *Annu. Rev. Neurosci.* *36*, 451–466.
- Takesian, A.E., Bogart, L.J., Lichtman, J.W., and Hensch, T.K. (2018). Inhibitory circuit gating of auditory critical-period plasticity. *Nat. Neurosci.* *21*, 218–227.
- Tasic, B., Menon, V., Nguyen, T.N., Kim, T.K., Jarsky, T., Yao, Z., Levi, B., Gray, L.T., Sorensen, S.A., Dolbeare, T., et al. (2016). Adult mouse cortical cell taxonomy revealed by single cell transcriptomics. *Nat. Neurosci.* *19*, 335–346.
- Tasic, B., Yao, Z., Graybiuck, L.T., Smith, K.A., Nguyen, T.N., Bertagnolli, D., Goldy, J., Garren, E., Economo, M.N., Viswanathan, S., et al. (2018). Shared and distinct transcriptomic cell types across neocortical areas. *Nature* *563*, 72–78.
- Ting, J.T., Lee, B.R., Chong, P., Soler-Llavina, G., Cobbs, C., Koch, C., Zeng, H., and Lein, E. (2018). Preparation of Acute Brain Slices Using an Optimized N-Methyl-D-glucamine Protective Recovery Method. *J. Vis. Exp.* 53825.
- Tuncdemir, S.N., Wamsley, B., Stam, F.J., Osakada, F., Goulding, M., Callaway, E.M., Rudy, B., and Fishell, G. (2016). Early Somatostatin Interneuron Connectivity Mediates the Maturation of Deep Layer Cortical Circuits. *Neuron* *89*, 521–535.
- Vormstein-Schneider, D., Lin, J.D., Pelkey, K.A., Chittajallu, R., Guo, B., Arias-Garcia, M.A., Allaway, K., Sakopoulos, S., Schneider, G., Stevenson, O., et al. (2020). Viral manipulation of functionally distinct interneurons in mice, non-human primates and humans. *Nat. Neurosci.* *23*, 1629–1636.
- Wickersham, I.R., Lyon, D.C., Barnard, R.J., Mori, T., Finke, S., Conzelmann, K.K., Young, J.A., and Callaway, E.M. (2007). Monosynaptic restriction of transsynaptic tracing from single, genetically targeted neurons. *Neuron* *53*, 639–647.
- Williams, A.L., Reese, B.E., and Jeffery, G. (2002). Role of retinal afferents in regulating growth and shape of the lateral geniculate nucleus. *J. Comp. Neurol.* *445*, 269–277.
- Zhang, S., Xu, M., Kamigaki, T., Hoang Do, J.P., Chang, W.C., Jenvay, S., Miyamichi, K., Luo, L., and Dan, Y. (2014). Selective attention. Long-range and local circuits for top-down modulation of visual cortex processing. *Science* *345*, 660–665.
- Zhu, Y., and Zhu, J.J. (2004). Rapid arrival and integration of ascending sensory information in layer 1 nonpyramidal neurons and tuft dendrites of layer 5 pyramidal neurons of the neocortex. *J. Neurosci.* *24*, 1272–1279.
- Zhuang, J., Larsen, R.S., Takasaki, K.T., Ouellette, N.D., Daigle, T.L., Tasic, B., Waters, J., Zeng, H., and Reid, R.C. (2019). The spatial structure of feedforward information in mouse primary visual cortex. *R. S. Larsen. bioRxiv*. <https://doi.org/10.1101/2019.12.24.888156>.
- Zingg, B., Hintiryan, H., Gou, L., Song, M.Y., Bay, M., Bienkowski, M.S., Foster, N.N., Yamashita, S., Bowman, I., Toga, A.W., and Dong, H.W. (2014). Neural networks of the mouse neocortex. *Cell* *156*, 1096–1111.
- Zingg, B., Chou, X.L., Zhang, Z.G., Mesik, L., Liang, F., Tao, H.W., and Zhang, L.I. (2017). AAV-Mediated Anterograde Transsynaptic Tagging: Mapping Corticocollicular Input-Defined Neural Pathways for Defense Behaviors. *Neuron* *93*, 33–47.

STAR★METHODS

KEY RESOURCES TABLE

REAGENT or RESOURCE	SOURCE	IDENTIFIER
Antibodies		
Mouse monoclonal IgG2a anti-Channelrhodopsin 2	ARP	Cat# 03-651180, clone 1500; RRID:AB_2892521
Chicken anti-GFP	Aves labs	Cat# 1020 RRID:AB_10000240
Goat anti-mCherry	Sicgen	Cat# AB0040 RRID:AB_2333093
Donkey anti-chicken 488	Jackson Immunoresearch	Cat# 703-545-155 RRID:AB_2340375
Goat anti-mouse IgG2a 555	ThermoFisher Scientific	Cat# A-21137 RRID:AB_2535776
Donkey anti-goat 594	ThermoFisher Scientific	Cat# A-11058 RRID:AB_2534105
Streptavidin-647	ThermoFisher Scientific	Cat # S32357 RRID:AB_2892522
Guinee pig anti-NeuN	Millipore Sigma	Cat # ABN90 RRID:AB_11205592
Bacterial and virus strains		
AAV-DIO-N2C-G-P2A-TVA-P2A-eGFP	Pouchelon et al., 2020	N/A
EnvA-CVS-N2C(DG)-FlpO-mCherry	Pouchelon et al., 2020	N/A
AAV-hSyn-hChr2(H134R)-EYFP	Boyden et al., 2005	Karl Deisseroth: Addgene_26973-AAV1 RRID:Addgene_26973-AAV1
AAV-EF1a-DIO-hChr2-eYFP	Boyden et al., 2005	Karl Deisseroth: Addgene_20298 RRID:Addgene_20298
AAV-hSyn-fDIO-DTA	This paper	N/A
AAV2/1-Ef1a-fDIO-hChr2-eYFP	Fenno et al., 2014	Karl Deisseroth: Addgene_55639 RRID:Addgene_55639
pENN-AAV2/1-CamKII-Cre.SV40	Gift from James Wilson	James Wilson: Addgene_105558 RRID:Addgene_105558
AAV (PHP-eB)-S5E2-GFP	Vormstein-Schneider et al., 2020	Jordane Dimidschtein: Addgene_135631 RRID:Addgene_135631
hSyn-DIO-hM4D(Gi)-tagBFP	This paper	N/A
AAV-hSyn-DIO-hM3D(Gq)-mCherry	Krashes et al., 2011	Bryan Roth: Addgene_44361-PHP-eB RRID:Addgene_44361-PHP-eB
AAV-hSyn-hM3D(Gq)-mCherry	Gift from Bryan Roth	Bryan Roth: Addgene_50475-AAV2 RRID:Addgene_50475-AAV2
Chemicals, peptides, and recombinant proteins		
Clozapine-N-Oxide	Tocris Bioscience	Cat. No. 4936
Tetrodotoxin	Tocris Bioscience	Cat. No. 1078
4-Aminopyridine	Tocris Bioscience	Cat. No. 0940
Experimental models: Organisms/strains		
Mouse: B6.Cg-Ndn ^{tm1.1(floA)cre^{Hze}/J}	Jackson Laboratories	Cat. No. 028536 RRID:IMSR_JAX:028536
Mouse: B6.Cg-Vipr2 ^{em1.1(cre)Hze} /J	Jackson Laboratories	Cat. No. 031332 RRID:IMSR_JAX:031332
Mouse: B6.Cg-Gt(ROSA) ^{26Sor^{tm14(CAG-tgTomato)Hze}/J}	Jackson Laboratories	Cat. No. 007914 RRID:IMSR_JAX:007914
Mouse: B6;C3-Tg(Scnn1a-cre)3Aibs/J	Jackson Laboratories	Cat. No. 009613 RRID:IMSR_JAX:009613
Mouse: B6.FVB-Tg(Npy-hrGFP)1Lowl/J	Jackson Laboratories	Cat. No. 006417 RRID:IMSR_JAX:006417
Mouse: B6.Sst ^{tm2.1(cre)Zjh} /J	Jackson Laboratories	Cat. No. 013044 RRID:IMSR_JAX:013044
Mouse: B6.Vip ^{tm1(cre)Zjh} /J	Jackson Laboratories	Cat. No. 010908 RRID:IMSR_JAX:010908
Mouse: B6;129-Gt(ROSA) ^{26Sor^{tm5(CAG-Sun1(stGFP)Nat}/J}	Jackson Laboratories	Cat. No. 021039 RRID:IMSR_JAX:021039
B6.129P2-Pvalb ^{tm1(cre)Arbr} /J	Jackson Laboratories	Cat. No. 017320 RRID:IMSR_JAX:017320

(Continued on next page)

REAGENT or RESOURCE	SOURCE	IDENTIFIER
Continued		
Recombinant DNA		
CVS-N2c(DG)-mCherry-P2A-FlpO	Reardon et al., 2016	Thomas Jessel; Addgene_73471 RRID:Addgene_73471
VTKS1 backbone	NYUAD	Addgene_170852
VTKS2 backbone	NYUAD	Addgene_170853
VTKS3 backbone	NYUAD	Addgene_170854
Software and algorithms		
Clampfit 10.7 (pClamp)	Molecular Devices	https://www.moleculardevices.com/products/software/pclamp.html ; RRID:SCR_011323
Easy Electrophysiology V2	Easy Electrophysiology	https://www.easyelectrophysiology.com/ ; RRID:SCR_021190
Prism 9.1.2	Graphpad Software	https://www.graphpad.com:443/ ; RRID:SCR_002798
Zen Blue 2.6	Zeiss	https://www.zeiss.com/microscopy/en_us/products/microscope-software/zen.html ; RRID:SCR_013672
NeuroLucida 360	MBF Bioscience	https://www.mbfioscience.com/neuroLucida360 ; RRID:SCR_016788
ImageJ 2.0.0 Java 1.8.0_66	National Institute of Health	https://imagej.net/ ; RRID:SCR_003070

RESOURCE AVAILABILITY

Lead contact

Further information and requests for reagent should be directed to the lead contact Gord Fishell (gordon_fishell@hms.harvard.edu)

Materials availability

Plasmids and viruses created in this study are available upon request from the lead contact.

Data and code availability

- Microscopy and electrophysiology data reported in this paper will be shared by the lead contact upon request.
- Software used for data analysis are included in the [Key resources table](#)
- Any additional information required to reanalyze the data reported in this work paper is available from the Lead Contact upon request.

EXPERIMENTAL MODEL AND SUBJECT DETAILS

Mice

All experiments were approved by and in accordance with Harvard Medical School IACUC protocol number IS00001269. C57BL/6 mice were used for breeding with transgenic mice. Transgenic mice, NDNF-dgCre (Jax stock number: 028536), Vipr2-IRES-Cre-D (stock number: 031332), Scnn1a-Tg3-Cre (Jax stock number: 009613), VIP-IRES-Cre (Jax stock #010908), PV-IRES-Cre (Jax stock #017320), SST-IRES-Cre (Jax stock # #013044), Ai14 (Jax stock number: 007909), Sun1-GFP (Jax stock #021039) are available at Jackson Laboratories. Animals were group housed and maintained under standard, temperature-controlled laboratory conditions. Mice were kept on a 12:12 light/dark cycle and received water and food *ad libitum*. For experiments during development, mice were injected at ~P1 and experiments conducted between ages P13–P15. In the case of adults, mice were injected at P30, and experiments conducted between ages P45–P50. Both female and male were used in the entire study and similar results were obtained in both sexes.

METHOD DETAILS

Sensory deprivations

To deprive mice from visual sensory input, enucleation was performed. P4 mouse pups were anesthetized by hypothermia. A small incision was made between the eyelids with a scalpel and the eye was separated from the optic nerve with micro-scissors to be

removed from the orbit. The incision was secured using biocompatible Vetbond glue. The pups were then allowed to recover on a heating pad before being returned to their mother. Dark rearing was performed by putting the cage (mom with P4 pups) in a tightly dark chamber, where temperature and humidity were controlled. Mice were monitored on a daily basis (in the dark) to make sure they have adequate food and water.

Histology

Mice between P42-P46 for the adult time point or P15 for the developmental time point were transcardially perfused with 4% paraformaldehyde (PFA) and brains were fixed overnight in 4% PFA at 4 °C. 50 μ m vibratome sections were used for all histological experiments. Every 3rd representative section was collected, and the sections were processed for immunohistochemistry. For immunofluorescence, brain sections were incubated for 1 h at room temperature in a blocking solution containing 10% normal donkey serum (NDS) and 0.3% Triton X-100 in PBS and incubated overnight at 4°C with primary antibodies: goat anti-mCherry (1:1,000; SicGen), chicken anti-GFP (1:1000; Aves Labs #1020) and/or mouse IgG2A anti-ChR2 (1:200; ARP Inc). Sections were rinsed three times in PBS and incubated for 60–90 min at room temperature or overnight at 4°C with the Alexa Fluor 488- and 594- and 647-conjugated secondary antibodies (1:500; Thermo Fisher Science or Jackson ImmunoResearch).

For L1 IN morphology, cells filled with biocytin were stained with Streptavidin-conjugated with Alexa 647. Briefly, recorded sections were postfixed with 4% PFA overnight, rinsed in PBS, cleared in Cubic1 solution (as described in (Schuman et al., 2018, 2019), blocked with Normal Donkey Serum and stained with Streptavidin-647 (1:500, ThermoFisher Scientific Cat # S32357) and anti-GFP (to visualize ACC fibers). The sections were then washed, cleared in Cubic2 solution and mounted for confocal imaging using Zeiss LSM 800 microscope.

Rabies tracing

For tracing afferents from NDNF+ neurons in V1, stereotactic injections were performed between P30-P35 in the case of adult mice. AAV-helpers (Titer of 9.5×10^{12} vg/mL) and N2c-RV-mCherry were diluted with PBS at a ratio of 1:1 and 50nL was injected using NanojectIII at the rate of 1nL/s in V1 (AP-3.5mm, ML-2.5mm, DV-0.20mm). Animals were perfused 14 days later. For developmental time points, stereotaxic injections were performed using a neonate adaptor (Harvard apparatus). Mouse pups were anesthetized by hypothermia and stereotaxically injected with the viruses at P1 (From Lambda: AP+0.2mm, ML-1.60mm, DV-0.1mm). Animals were perfused 14 days later at P15. All coordinates were determined to target mainly L1 of the cortex. In the case of RV tracing from L4 neurons, AAV helper and RV were injected at a depth of DV-0.5mm.

Viruses

For rabies tracing

AAV2/1-DIO-helper virus encoding N2c-G-P2A-TVA-P2A-eGFP (NYUAD and designed from VTKS2 backbone Addgene #170853) was expressed in a single AAV vector as described in (Pouchelon et al., 2020). EnvA-pseudotyped CVS-N2c(Δ G)-FlpO-mCherry was used. The RV CVS-N2c(Δ G)-mCherry-P2A-FlpO was a gift from Thomas Jessell (Addgene plasmid # 73471; (Reardon et al., 2016) and the N2c-RV were either produced, amplified and EnvA-pseudotyped in the lab, or generously shared by K. Ritola at Janelia Farms Research Center.

Other viruses used in the paper

AAV2/1-hSyn-hChR2(H134R)-EYFP was a gift from Karl Deisseroth (Addgene #26973-AAV1; (Boyden et al., 2005); AAV2/1-hSyn-hM3D(Gq)-mCherry was a gift from Bryan Roth (Addgene #50474-AAV2; (Krashes et al., 2011); AAV(PHP-eb)-hSyn-DIO-hM3D(Gq)-mCherry was a gift from Bryan Roth (Addgene #44361-PHP-eb); AAV2/1-Ef1a-fDIO-hChr2-eYFP was a gift from Karl Deisseroth (Addgene #55639-AAV1; (Fenno et al., 2014); pAAV2/1-EF1a-DIO-hChR2-eYFP/mCherry was a gift from Karl Deisseroth (Addgene #20298/20297-AAV1); AAV2/1-hSyn-fDIO-DTA (NYUAD, designed from VTKS3 backbone, Addgene #170854); AAV2/1-hSyn-DIO-hM4D(Gi)-tagBFP (NYUAD, designed from VTKS2 backbone, Addgene #170853). pENN-AAV2/1-CamKII-Cre.SV40 was a gift from James Wilson (Addgene #105558). AAV (PHP-eb)-S5E2-GFP was a gift from Jordane Dimidschtein (Addgene #135631; (Vormstein-Schneider et al., 2020).

Trans-synaptic labeling

Retina Injections

1.5 μ l of pENN-AAV2/1-CamKII-Cre.SV40 (Titer of 1×10^{13} vg/mL) was injected in the right retina (750nL in dorsal and 750nL in ventral retina).

dLGN injections

700nL of pAAV2/1-EF1a-DIO-hChR2-mCherry (Titer of 5×10^{12} vg/mL) was injected into the contralateral dLGN spread over 3 different depths to cover the dLGN (2.2mm, -2.3mm, 2.5-2.75mm).

Image analysis

Each brain section containing labeled cells was acquired as a tiled image on a motorized tiling scope Zeiss Axio Imager A1. Starter cells (colocalization of GFP⁺ AAV-helpers and mCherry⁺ RV) were manually quantified on ImageJ software. Brains with more than 10 non-L1 starter cells were not included in the analysis. mCherry⁺ retrogradely labeled cells were registered for each region of the Allen

Reference Brain atlas for adult brain and of the “Atlas of Developing Mouse Brain at P6” from George Paxinos 2006. The number of retrogradely labeled cells in a given region were normalized to the total number of cells labeled in the entire brain for the analysis in Figure 1E; to the total number of retrogradely labeled cells within V1 (Figures S1A and S1B) or to the total number of retrogradely labeled cells in the visual thalamus (Figures S1C and S1D).

Stereotaxic Injections for optogenetics and slice recording

For ACC injections

80nL of 1:1 dilution (with PBS) of AAV1-hSyn-hChR2(H134R)-eYFP (Titer of 1×10^{13} vg/mL) was injected in the left ACC using the following coordinates for adult [AP 0.5mm, ML 0.35mm, DV 0.5mm], and for development (50nL 1:1 dilution [From Lambda: AP 2mm, ML 0.2mm, DV 0.5mm]).

For RSP injections

the following coordinates were used for developmental time point [From Lambda: AP 1.4mm, ML 0.2mm, DV 0.5mm] and for adults [AP -2mm, ML 0.5mm, DV 0.5mm].

For dLGN injections

50nL AAV1-EF1a-DIO-hChR2(H134R)-eYFP was injected in the left dLGN of *Vipr2-IRES-Cre-D* mice using stereotaxic injection at P1 for developmental time point [From Lambda: AP 0.8mm, ML 1.3mm, DV 1.4mm]. Either WT mice injected with AAV1-hSyn-hChR2(H134R)-eYFP (100nL 5×10^{12} vg/mL) or *Vipr2-IRES-Cre-D* mice were injected with AAV1-EF1a-DIO-hChR2(H134R)-eYFP (100nL 5×10^{12} vg/mL) at ~P30-35 for the adult time point [AP -2.3mm, ML 2.2mm, DV 2.6mm].

Animal selection criteria

Mice with non-uniform or non-specific injections in either ACC or dLGN were excluded from the study.

In the case of PV INs recording, either PV-Cre::Sun1-GFP mice were used; or PV neurons were labeled using an AAV with a PV-specific enhancer (S5E2; [Vormstein-Schneider et al., 2020](#))

In vitro electrophysiology

P13-P15 were decapitated, and the brain was quickly removed and immersed in ice-cold oxygenated (95% O₂ / 5% CO₂) sucrose cutting solution containing 87 mM NaCl, 2.5 mM KCl, 2 mM MgCl₂, 1 mM CaCl₂, 1.25 mM NaH₂PO₄, 26 mM NaHCO₃, 10 mM glucose and 75 mM sucrose (pH 7.4). 300 μm thick coronal slices were cut using a Leica VT 1200S vibratome through V1. Slices were recovered in a holding chamber with artificial cerebrospinal fluid (aCSF) containing 124 mM NaCl, 20 mM Glucose, 3 mM KCl, 1.2 mM NaH₂PO₄, 26 mM NaHCO₃, 2 mM CaCl₂, 1 mM MgCl₂ (pH 7.4) at 34°C for 30 minutes and at room temperature for at least 45 minutes prior to recordings. For adult recordings, mice were perfused with NMDG cutting solution containing 92mM NMDG, 2.5mM KCl, 1.2mM NaH₂PO₄, 30mM NaHCO₃, 20mM HEPES, 25mM glucose, 5mM sodium ascorbate, 3mM sodium pyruvate, 0.5mM CaCl₂, 10mM MgSO₄. During recovery, the NaCl was gradually added as described in [Ting et al. \(2018\)](#). For recordings, slices were transferred to an upright microscope (Zeiss) with IR-DIC optics. Cells were visualized using a 40x water immersion objective. Slices were perfused with aCSF in a recording chamber at 2 mL/min at 30°C. All slice preparation and recording solutions were oxygenated with carbogen gas (95% O₂, 5% CO₂, pH 7.4). Patch electrodes (3–6 MΩ) were pulled from borosilicate glass (1.5 mm OD, Harvard Apparatus). For all recordings patch pipettes were filled with an internal solution containing: 125 mM Cs-gluconate, 2 mM CsCl, 10 mM HEPES, 1 mM EGTA, 4 mM MgATP, 0.3 mM NaGTP, 8 mM Phosphocreatine-Tris, 1 mM QX-314-Cl, equilibrated with CsOH at pH 7.3 or 130 K-Gluconate, 10 KCl, 10 HEPES, 0.2 EGTA, 4 MgATP, 0.3 NaGTP, 5 Phosphocreatine and 0.4% biocytin, equilibrated with KOH CO₂ to a pH = 7.3.

Recordings were performed using a Multiclamp 700B amplifier (Molecular Devices) and digitized using a Digidata 1440A and the Clampex 10 program suite (Molecular Devices). Voltage-clamp signals were filtered at 3 kHz and recorded with a sampling rate of 10 kHz. Recordings were performed at a holding potential of -70 mV. Cells were only accepted for analysis if the initial series resistance was less than 40 MΩ and did not change by more than 20% during the recording period. The series resistance was compensated at least ~30% in voltage-clamp mode and no correction were made for the liquid junction potential. Whole-cell patch-clamp recordings were obtained from L1 INs and pyramidal-shaped neurons in L2/3 or L4 located in the same column. To activate afferents expressing hChR2, blue light was transmitted from a collimated LED (Mightex) attached to the epifluorescence port of the upright microscope. 5ms or 1ms pulses of a fixed light intensity were directed to the slice in the recording chamber via a mirror coupled to the 40x objective. Flashes were delivered every 15 s for a total of 10 trials. The LED output was driven by a transistor-transistor logic output from the Clampex software. In some cases, recordings were performed in the presence of 1 μM TTX and 1 mM 4-AP (Tocris) (after identifying cell type without drugs) to reveal pure monosynaptic inputs. We only used cells that were monosynaptic based on latency of the response, which was found to be 3ms on average from the start of the light stimulation.

None of the experiments were blinded to the conditions. In some cases, a different experimenter confirmed the findings.

Data Analysis

Passive and active membrane properties were recorded in current clamp mode by applying a series of hyperpolarizing and depolarizing current steps. All intrinsic physiological properties were analyzed using Clampfit10.7 and Easy Electrophysiology V2.2. The Resting membrane potential was recorded soon after break-in at $I = 0$. The cell input resistance was calculated from the peak of the voltage response to a 200pA hyperpolarizing 1 s-long current step according to Ohm's law. The sag or hump peak voltage deflection is calculated as the difference between peak membrane potential and baseline based on a 200pA

hyperpolarizing current injection. Analysis of the action potential properties was done on the first spike observed during a series of depolarizing steps. Threshold was defined as the voltage at the point when the slope first exceeds a value of 20 V s^{-1} . Rheobase was defined as the amplitude of the first depolarizing current step at which firing was observed. Spike half width is defined as the width at half amplitude. Fast hyperpolarization (fAHP) is calculated as the difference between spike threshold and minimum the voltage after the spike within 3ms. Medium afterhyperpolarization (mAHP) is defined as difference between spike threshold and minimum voltage after the spike, from 10 to 50ms.

Analysis of spontaneous inhibitory events was done using Clampfit's threshold search.

For optogenetic experiments, data analysis was performed offline using the Clampfit 10.7 module of pClamp (Molecular Devices) and Prism 8 (GraphPad). The amplitude of evoked synaptic currents to 5ms blue-light stimulation was obtained by averaging the peak amplitude of individual waveforms over 10 trials per cell. EPSC amplitudes recorded from L1 INs were then normalized for injection size by dividing the average EPSC by the evoked current amplitude from a putative L2/3 or L4 pyramidal neuron in the same column of each slice. Failure rate was computed as the percentage of trials that evoked no response of any amplitude in response to a 1ms blue-light stimulation.

CNO injections

CNO (diluted in DMSO and saline, Tocris Cat #4936) was injected at a concentration of 0.01mg/kg of body weight and was injected daily starting at either P5 or P11, until recording day (P13-P15). Injections were made in the milk sac of the pups, and later injections were made intraperitoneally.

NeuroLucida tracing

Sections containing the axons of interest were imaged on a Zeiss LSM 800. Z stacks of images were then loaded into NeuroLucida 360 (MBF Biosciences) and trees were reconstructed using the 'user guided' option with Directional Kernels.

QUANTIFICATION AND STATISTICAL ANALYSIS

No prior test for determining sample size was conducted. All statistical analyses were performed using Prism (GraphPad). Statistical significance was tested with non-paired, two-sided t test, with a 95% confidence interval or One-Way ANOVA with Tukey's correction for multiple comparisons. In some cases, One-Way ANOVA with Brown-Forsythe test was used in the cases where SD was not equal. All data are presented as mean \pm SEM unless otherwise stated. Across the manuscript, N refers to number of animals, whereas n refers to number of cells. This information is included in the legends for each figure.